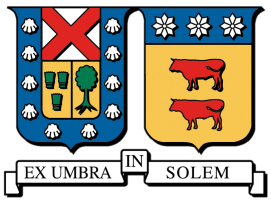

Universidad Técnica Federico Santa María

Master Thesis

Active Phase Stabilization of a Distance-Scalable Fiber-Optic Interferometer

Author:
Yerko A. Muñoz Barros

Supervisor:
Dr. William Brooks

Co-supervisor:
Cristián Peña

A thesis submitted in fulfillment of the requirements for the degree of Master of Science in Physics

in the Department of Physics

March 17, 2026

CONSTANCIA DE VALIDACIÓN Y CONFIDENCIALIDAD DE MONOGRAFÍA A REPOSITORIO ACADÉMICO

1.- IDENTIFICACIÓN DEL TRABAJO ACADÉMICO

Tipo de monografía (marcar una opción): ☐ Memoria o trabajo de título ☒Tesis de Postgrado

Título del trabajo: Active Phase Stabilization of a Distance-Scalable Fiber-Optic Interferometer

Nombre del candidato(a): Yerko Agustín Muñoz Barros

Carrera / Grado: Magíster en Ciencias mención Física

Campus: Casa Central **Departamento:** Departamento de Física

2.- VALIDACIÓN DEL PROFESOR GUÍA/DIRECTOR DE TESIS

Yo, **William King Brooks**, en mi calidad de profesor(a) guía/director(a) del trabajo académico mencionado anteriormente **DEJO CONSTANCIA** que:

- He revisado esta versión del documento y corresponde a la versión final aprobada del trabajo.
- El trabajo cumple con los requisitos académicos y de formato establecidos por la institución.

3.- EVALUACIÓN DE CONFIDENCIALIDAD POR PROPIEDAD INDUSTRIAL (marcar una opción)

☒ El trabajo **NO contiene** información que amerite confidencialidad y puede ser publicado de inmediato en repositorio con acceso abierto.

☐ El trabajo **CONTIENE** información con potenciales implicancias de propiedad industrial o intelectual y requiere un periodo de confidencialidad (**embargo**) por **(marcar una opción)**:

☐ 6 meses ☐ 12 meses ☐ 2 años ☐ 3 años ☐ 5 años ☐ 10 años

Fundamentación de la necesidad de confidencialidad (obligatorio si se solicita embargo):

4.- FIRMAS

Profesor(a) guía o director(a) de memoria o tesis:

Fecha: 17/03/2026 **Firma:** William King Brooks

Estudiante o Candidato(a):

Fecha: 17/03/2026 **Firma:**

Este formulario debe ser insertado como página 2 de la memoria o tesis, completado y firmado por estudiante y profesor(a) antes de la entrega en portal PRISMA de Biblioteca USM.

"*I ain't no physicist, but I know what matters.*"

Popeye The Sailor

UNIVERSIDAD TÉCNICA FEDERICO SANTA MARÍA

Abstract

Department of Physics

Master of Science in Physics

Active Phase Stabilization of a Distance-Scalable Fiber-Optic Interferometer

by Yerko A. Muñoz Barros

We present the design and implementation of an active phase-stabilization system for a distance-scalable Mach-Zehnder interferometer aimed to incorporate a 10.8 km underground optical fiber link at Fermilab. The system employs a coherent self-homodyne detection scheme with a 90-degree optical hybrid to generate In-phase (I) and Quadrature (Q) signals, which provide an error signal for a high-bandwidth feedback loop. A low-latency, Field-Programmable Gate Array (FPGA) controller executes a Proportional-Integral-Derivative (PID) control algorithm, applying real-time phase corrections via an Electro-Optic Modulator (EOM) to counteract environmental phase noise. We present a full characterization of the free-drifting phase noise and demonstrate a significant reduction, quantified by using its standard deviation and Power Spectral Densities (PSDs). The successful implementation of this feedback system is expected to achieve robust, long-term phase locking, establishing a stable interferometric platform for future quantum networking experiments and many other applications requiring precise phase control over long fiber links.

Acknowledgements

I would like to express my deepest gratitude to my supervisor, Dr. William Brooks, for his trust and guidance throughout the process of sending me to Fermilab to conduct this research. There, Dr. Cristian Peña and Dr. Andrew Cameron provided invaluable support, feedback and mentorship, helping me navigate the complexities of the experimental setup and theoretical background on a topic unknown to me when I joined the project. I am also grateful to the entire science group at Fermilab for their collaborative spirit and insightful discussions that enriched this work, specifically to the QICK team and specially to Dr. Horacio Arnaldi for his hekp with the FPGA programming and control system design.

Finally, I want to thank my family, friends and my loved one, for their unwavering support and encouragement during this journey. This thesis would not have been possible without the collective efforts and support of all these individuals, to whom I am profoundly thankful.

Contents

List of Figures

List of Tables

Acronyms

BB84 Bennett-Brassard 1984 . . . . . pp. 4, 36

CHARA Center for High Angular Resolution Astronomy . . . . . p. 7

CW Continuous Wave . . . . . p. 23

DAC Digital-to-Analog Converter . . . . . p. 19

EOM Electro-Optic Modulator . . . . . pp. v, 9, 11, 18–21, 23–25, 28–30, 35

FPC Fiber Polarization Controller . . . . . p. 24

FPGA Field-Programmable Gate Array . . . pp. v, 9, 11, 19, 20, 23, 25, 29, 30, 35

LIGO Laser Interferometer Gravitational-Wave Observatory . . . . . p. 6

LO Local Oscillator . . . . . pp. 15, 16, 23, 25

MZI Mach-Zehnder Interferometer . . . . . pp. 9, 11, 12, 15, 17, 21, 23, 35

OPD Optical Path Difference . . . . . pp. 6, 8

PBS Polarizing Beam Splitter . . . . . p. 24

PID Proportional-Integral-Derivative . . . . . pp. v, 9, 18, 20, 21, 29, 30, 35, 36

PM Power Meter . . . . . p. 24

PNS Photon Number Splitting . . . . . p. 4

PSD Power Spectral Density . . . . . pp. v, 26–28, 31, 33, 35

QBER Quantum Bit Error Rate . . . . . p. 36

QICK Quantum Instrumentation Control Kit . . . . . p. 20

QKD Quantum Key Distribution . . . . . pp. 4, 36

RMS Root Mean Square . . . . . pp. 27, 28

RSA Rivest-Shamir-Adleman . . . . . p. 3

TF-QKD Twin-Field Quantum Key Distribution . . . . . pp. 5, 6, 8, 36

VLTI Very Large Telescope Interferometer . . . . . pp. 7, 8

WCP Weak Coherent Pulse . . . . . pp. 4, 5

Chapter 1

Introduction

1.1 The Need for Phase Stability in Modern Physics

The evolution of physical science in the last century can be distinctly categorized into two epochs. The "First Quantum Revolution" arose at the turn of the 20th century, driven by theoretical necessities to explain anomalies such as blackbody radiation and the photoelectric effect. Here is when Einstein introduced the concept of photons or quantized light, proposing that light could be thought of as discrete packets of energy, or "quanta". This era established the fundamental tenets of wave-particle duality: the recognition that matter exhibits wave-like characteristics and that light possesses particle-like quantization. This framework allowed for the comprehension of naturally occurring quantum phenomena, elucidating the periodic table, chemical bonding, and the electronic band structures that govern semiconductor physics [1, 2].

Technologically, this first revolution was characterized by the exploitation of collective quantum effects. The development of the transistor, the laser, and the integrated circuit relied on the statistical behavior of vast ensembles of electrons and photons [3, 4, 5]. While these technologies lead the Information Age [6], they rely on quantum mechanics for their explanation. We were effectively passive observers, exploiting the natural behaviors of quantum laws without manipulating individual quantum states.

We are now in the "Second Quantum Revolution" [7]. This paradigm shift is defined not by observation, but by the active engineering of the quantum world. The objective is no longer solely to miniaturize classical devices to the nanoscale, but to develop technologies that explicitly leverage the non-classical properties of superposition and entanglement. Rather than managing ensembles, we now isolate, control, and measure individual quantum systems, such as trapped ions, superconducting circuits, or single photons [8, 9]. Photons are now viewed as individual quantum objects that can be manipulated and controlled, paving the way for new applications in quantum information science. This transition from descriptive science to applied engineering allows for the creation of artificial quantum states with no natural analogue, offering unprecedented capabilities in computation, secure communication, and metrology [10, 11].

However, the transition from classical to quantum engineering introduces a rigorous constraint: phase stability. The distributed photon technologies can be integrated with existing optical fiber infrastructure but they are inherently sensitive to phase noise, which can arise from various environmental factors. Much like the second quantum revolution has been built around the control of single particles, researchers nowadays require the same level of control of the medium that contains the quantum systems.

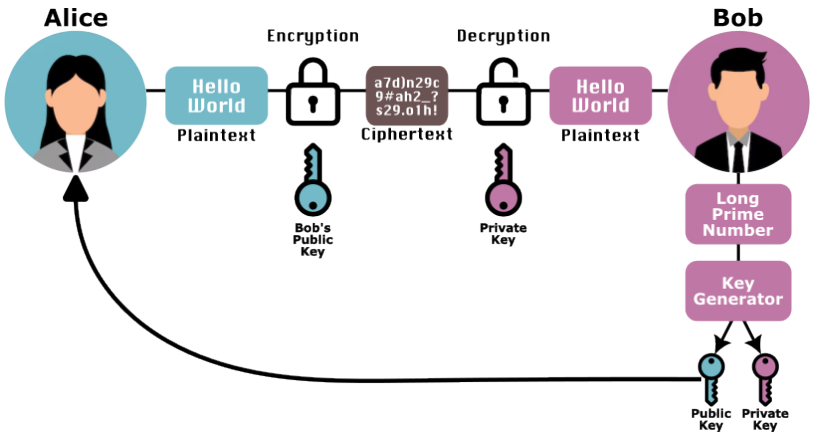

FIGURE 1.1: Asymmetric cryptography process between Alice and Bob using public and private keys.

In classical optics or communication, information is often encoded in intensity, which is robust against environmental fluctuations. In contrast, the advantage of quantum technology often lies in the coherent superposition of states. If we consider a general qubit state $|\psi\rangle = \alpha\,|0\rangle + e^{i\phi}\beta\,|1\rangle$, the relative phase ϕ between the basis states $|0\rangle$ and $|1\rangle$ is crucial. Any uncontrolled phase shift can lead to decoherence, effectively collapsing the superposition and destroying the quantum information encoded within. Therefore, maintaining phase stability is a fundamental requirement for the practical realization of quantum technologies, making the fight against phase noise a central challenge in the field.

Phase noise can arise from a variety of sources which we will explore in detail in Chapter 2. Phase stability is not only critical in quantum computing and communication, but also in precision measurement applications such as gravitational wave detections [12] and atomic clocks [13], and telescopes using interferometry. The next sections will delve deeper into the specific role of phase stability in these topics.

1.1.1 Quantum Networking

Most of the information we create and exchange today is in digital form and it keeps increasing exponentially every day. Recent analyses estimate that approximately 402.74 million terabytes of data are created daily as of the mid-2020s [14]. In this context, there are countless scenarios where secure and efficient communication is essential, from banking transactions to private communications, government operations, and general data management.

Cryptography is the science of secure communication and is a complex field that includes aspects of various disciplines, such as mathematics, computer science and information theory. To achieve such secure communication, we first need to talk about encryption, a fundamental component of cryptography, which involves transforming readable information (plaintext) into an unreadable format (ciphertext) using an algorithm and a key.

Encryption methods can be broadly classified into two categories based on the type of keys used: symmetric and asymmetric. For **asymmetric cryptography**, let's consider a practical example where two parties, Alice and Bob, wish to communicate securely. Bob generates a pair of keys: a public key and a private key. These keys are not really keys in the traditional sense, but rather large prime numbers that are

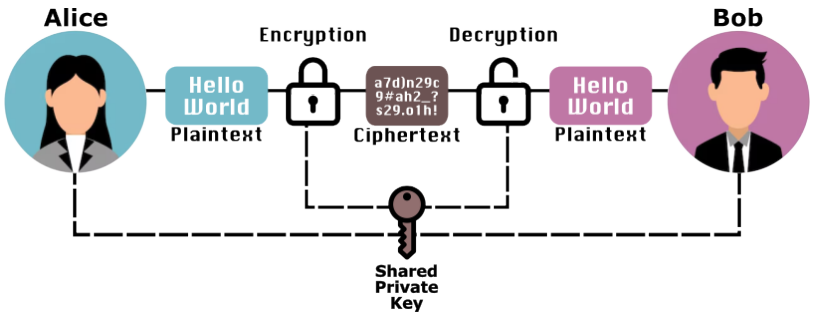

FIGURE 1.2: Symmetric cryptography process between Alice and Bob using a shared private key.

mathematically related to one another. In this case, related means that data encrypted with one key can only be decrypted with the other key. Bob shares his public key with Alice through a public channel (accessible to everyone), while keeping his private key secret. When Alice wants to send a message to Bob, she uses his public key to encrypt the message, transforming it into ciphertext. Once Bob receives the ciphertext, he uses his private key to decrypt it back into plaintext, accomplishing secure communication between the two parties. See Fig. 1.1 for a visual representation.

The most known and used method used to generate these related keys is the Rivest-Shamir-Adleman (RSA) algorithm [15], and its security is based on the assumption that, while it is easy to multiply two large prime numbers together to create a composite number, it is extremely difficult to reverse the process and factor the composite number back into its original prime components, a problem known as the *integer factorization problem* [16]. However, with the advent of quantum computing, these classical methods could quickly become vulnerable, since theoretically, quantum computers have been shown to have the potential to outperform classical ones when addressing integer factorization problems. Shor's algorithm demonstrates that a quantum computer can factor large integers exponentially faster than the best-known classical algorithms [17, 18]. A powerful quantum computer capable of running Shor's algorithm could break current encryption schemes in a fraction of the time required by today's computers, jeopardising the security of our current communications [19, 20].

To address this weakness of RSA, private key-based encryption schemes have emerged as a potential solution. Instead of relying on mathematical complexity for security, we rely purely on the secrecy of a long and random bit string shared key. This is the principle for **symmetric cryptography**, where both Alice and Bob share the same secret key used for both encryption and decryption (see Fig. 1.2). The main challenge with this, however, is the secure distribution of the key itself. If an eavesdropper, Eve, intercepts the key Alice sends to Bob during transmission, she can easily make a copy of it, send it back to Bob, and decrypt any messages sent between them without their knowledge.

To address this issue, we can take advantage of a direct consequence of quantum mechanics: it is not possible to create perfect copies of an unknown quantum state, a principle known as the *no-cloning* theorem [21]. For secure key transmission Alice can encode some information into single photons and send them to Bob over a quantum channel[1]. In this case, the intrinsic properties of quantum mechanics ensure that

[1] A quantum channel is simply the transmission route for quantum signals.

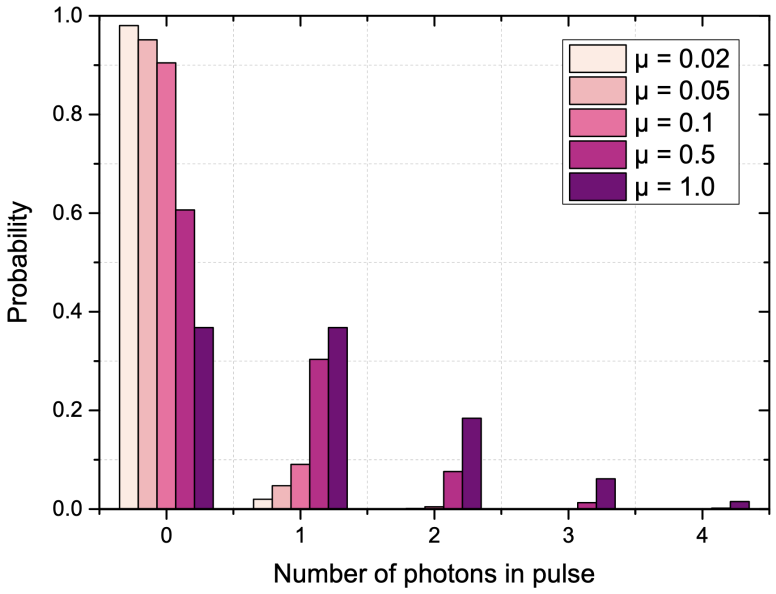

FIGURE 1.3: Photon number distribution in WCPs with different intensities (μ) [29]. CC BY-NC-SA 4.0.

any attempt by Eve to intercept and measure the photons will destroy their quantum superposition, introducing detectable anomalies that alert the two original communicating parties. This procedure of using quantum mechanics to securely distribute a key is known as Quantum Key Distribution (QKD), and its simplest protocol is the Bennett-Brassard 1984 (BB84) protocol, which uses the polarization states of single photons to encode information [22, 23].

While the BB84 protocol established the viability of QKD taking advantage of the no-cloning theorem, it remains constrained by practical limitations, since a single-photon source is required, a technology still in development. Most real-world implementations of QKD use Weak Coherent Pulses (WCPs) as an approximation of single-photon sources [24]. However, the photon statistics of WCPs follow a Poisson distribution $P(n) = e^{-\mu}\mu^n/n!$ (see Fig. 1.3), which introduces vulnerabilities to certain types of attacks, such as the Photon Number Splitting (PNS) attack [25]. In this attack, Eve could intercept the multi-photon pulse, split it, measure one photon to gain information about the key, and then forward the remaining photons to Bob without introducing detectable disturbances.

To mitigate the risks associated with WCPs, various strategies have been developed. One common approach is the decoy state method [26], where Alice randomly varies the intensity of the pulses she sends to Bob. Photons are transmitted by Alice using randomly chosen intensity levels (one signal state and several decoy states), making it impossible for Eve to determine which pulses contain multiple photons. If Eve were to attempt a PNS attack, she would change the intensity statistics of the received pulses, which Bob can detect by analyzing the detection rates corresponding to different intensity levels once Alice reveals them after transmission [27, 28].

This method significantly enhances the security of QKD systems using WCPs, but doesn't solve another fundamental limit: distance. The maximum distance over which secure QKD can be performed is limited by losses in the communication channel (e.g., optical fiber attenuation). As the distance increases linearly, the probability of

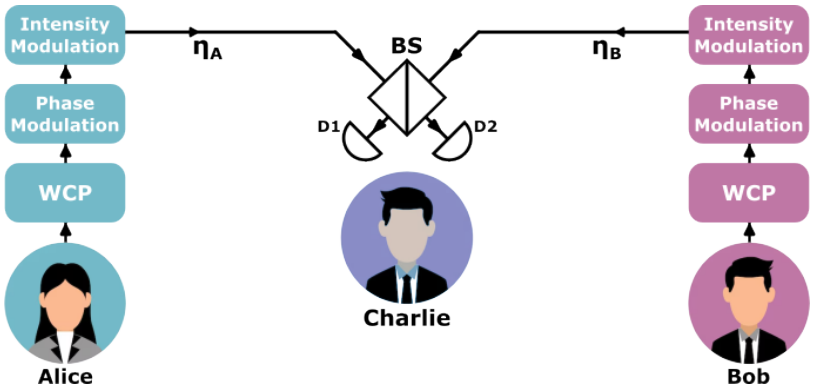

FIGURE 1.4: Schematic of a TF-QKD protocol. Alice and Bob send WCPs to an untrusted middle node, Charlie, who performs interference measurements.

photon loss increases exponentially, making the maximally achievable key distribution rates scale with the channel transmittance ($R \sim \eta$). In classical communication, signal amplification can be used, but in quantum communication, amplification is not possible without violating the no-cloning theorem [30]. This results in a fundamental limit known as the *repeaterless bound* which sets the maximum key rate achievable without quantum repeaters, a technology still in development [31, 32].

To overcome this limitation, the field advanced to Twin-Field Quantum Key Distribution (TF-QKD), a novel protocol that allows secure key distribution over much longer distances without the need for quantum repeaters [33]. In TF-QKD, both Alice and Bob send weak coherent pulses to a central untrusted node (Charlie) that interferes the incoming signals on a 50:50 beam splitter and detects the outcome using two single-photon detectors, exploiting first-order single-photon interference[2] (see Fig. 1.4). Consequently, assuming both paths transmittances are equal ($\eta_A = \eta_B = \eta$), this mechanism alters the scaling of the secure key rate with respect to the total channel transmittance from linear ($R \sim \eta$) to square-root ($R \sim \sqrt{\eta}$), since we only need one photon to survive the trip from either Alice or Bob to Charlie and not both [34].

In this protocol, the encoding of the photons is done in the relative phase between the WCPs sent by Alice and Bob, using two bases: $X : \{0, \pi\}$ and $Z : \{\frac{\pi}{2}, \frac{3\pi}{2}\}$. For example, consider the case where Alice and Bob encode bit values in the X-basis. If Alice prepares a pulse with phase $\phi_A = 0$ and Bob prepares a pulse with phase $\phi_B = 0$, the optical fields arrive at the beam splitter in phase. This results in constructive interference at one output port (e.g., corresponding to detector D_1) and destructive interference at the other (D_2). Conversely, if their phases differ by π (e.g., $\phi_A = 0$ and $\phi_B = \pi$), the interference conditions are swapped, causing D_2 to fire. Upon receiving Charlie's public announcement of the detection event, Alice and Bob share their bases and *sift* their results. That way, they can infer the parity of their bits without revealing the specific values: if D_1 clicked, they know their phases were identical; if D_2 clicked, their phases were opposite [33, 34].

However, the practical realization of this protocol rests entirely on the phase coherence and stability of the signals. Since TF-QKD effectively creates a large interferometer spanning the entire channel length, the optical phase difference between

[2]First-order single-photon interference demonstrates the wave nature of light at the most fundamental level, showing that individual photons interfere with themselves, not with other photons, by taking multiple paths simultaneously (superposition).

Alice and Bob must remain well defined during pulse transmission [33]. Even with perfectly prepared pulses, the microscopic length variation in either path is sufficient to prevent the high-visibility interference required for successful TF-QKD, so the system must employ active phase-stabilization mechanisms to track and compensate for these channel-induced phase drifts in real time [35], a challenge that we address in this work.

1.1.2 Precision Metrology

Beyond quantum communication, phase stability is equally central to some of the most ambitious measurement endeavors in modern science, including the gravitational wave detectors and atomic clocks mentioned above. Precision metrology, the discipline concerned with measuring physical quantities at the absolute limits of sensitivity, has long relied on interferometry as its primary tool, and interferometry is, at its core, a technology for converting phase information into measurable intensity signals.

The operating principle of any interferometer can be understood from the superposition of two optical fields. Consider two monochromatic fields of equal amplitude E_0 and angular frequency ω, traveling along two separate paths of lengths L_1 and L_2 before recombining at a detector. The total detected intensity at one output port is

$$I = \frac{E_0^2}{2}\left(1 + \cos\left(\Delta\phi\right)\right), \tag{1.1}$$

where $\Delta\phi = 2\pi\Delta L/\lambda$ is the phase difference corresponding to the Optical Path Difference (OPD) $\Delta L = L_1 - L_2$ [36]. This expression reveals both the power and the vulnerability of interferometric measurement: the intensity is exquisitely sensitive to changes in ΔL on the scale of the wavelength λ, but this same sensitivity means that any unintended perturbation to the path lengths, whether thermal, mechanical, or acoustic, directly contaminates the measurement as phase noise.

The most striking illustration of interferometry pushed to its ultimate limits is the detection of gravitational waves by the Laser Interferometer Gravitational-Wave Observatory (LIGO) [12]. LIGO operates as a Michelson interferometer with two perpendicular arms each 4 km long, in which laser light is bounced between suspended mirrors to build up an effective optical path length of approximately 1200 km. A passing gravitational wave stretches and compresses spacetime, producing a differential arm length change ΔL that the interferometer must resolve. The peak strain sensitivity of LIGO reaches $h \sim 10^{-23}\,\mathrm{Hz}^{-1/2}$, corresponding to an OPD sensitivity on the order of $10^{-19}\,\mathrm{m}$ [37], roughly one ten-thousandth the diameter of a proton. Achieving this requires that all phase fluctuations be suppressed far below this threshold through a complex setup of passive isolation and active control systems.

A complementary domain of precision metrology is timekeeping. Modern optical atomic clocks operate by locking a laser to an ultra-narrow electronic or optical transition in an atom or ion, with fractional frequency uncertainties now reaching below 10^{-18} [38, 39]. The clock transition itself acts as a phase reference: any drift in the laser frequency introduces a time-varying phase error that dephases the atomic superposition and degrades clock stability. The comparison and synchronization of such clocks over large distances requires the transmission of a phase-stable optical frequency reference over fiber links [40, 41]. This challenge of distributing a phase-coherent optical signal over a long deployed fiber is directly analogous to the one faced at the Fermilab underground link that motivates this work.

What unites these applications is a common mathematical structure. In each case, the quantity of interest — a gravitational wave strain, a clock frequency, a source visibility — is linearly encoded in the phase $\Delta\phi$ of an optical field. However, the output of any square-law detector is proportional to $\cos(\Delta\phi)$, as seen in Eq. 1.1, which is inherently nonlinear and sign-ambiguous: it cannot distinguish between $+\Delta\phi$ and $-\Delta\phi$, and its sensitivity vanishes entirely when $\Delta\phi \approx 0$ or π. Operating an interferometer as a linear, high-sensitivity phase transducer therefore requires resolving this ambiguity. The approach adopted in this work circumvents the problem: rather than locking to a fixed operating point, we employ hardware to extract components of the field. This provides the full complex phasor, from which the phase is recovered unambiguously via the four-quadrant arctangent [42], maintaining constant sensitivity regardless of the absolute phase value. The theoretical basis and practical implementation of this detection scheme are developed in detail in Chapter 2.

1.1.3 Telescopes and Imaging

A third domain in which phase stability emerges as a fundamental requirement is astronomical imaging, particularly in the context of multi-telescope optical interferometry. To understand why, it is instructive to first consider how a single telescope forms an image.

A conventional telescope operates as an intensity detector. The electromagnetic field arriving from a distant source carries both amplitude and phase information, but the photodetectors at the focal plane (whether photographic plates, CCDs, or infrared arrays) respond only to the time-averaged intensity of the incoming light, $I \propto \langle |E|^2 \rangle$. The phase of the optical field is therefore discarded in the detection process. For a single aperture, this is acceptable: the angular resolution of the telescope is diffraction-limited by its diameter D, yielding a resolving power of $\theta \sim \lambda/D$ [43]. To resolve finer angular features, such as the surface of a distant star or the environment surrounding a compact object, one must either increase the aperture or find an alternative means of recovering the spatial phase structure of the incoming wavefront.

The solution lies in *aperture synthesis interferometry*, a technique that coherently combines the light collected by two or more spatially separated telescopes. When two telescopes separated by a baseline B simultaneously observe the same source, the cross-correlation of their collected fields, known as the visibility [43], encodes information about the source's spatial structure at angular scales of λ/B. The fringe visibility is defined as

$$\mathcal{V} = \frac{I_{\max} - I_{\min}}{I_{\max} + I_{\min}}, \tag{1.2}$$

where $I_{\max}$ and $I_{\min}$ are the maximum and minimum intensities of the interference pattern. A visibility of $\mathcal{V} = 1$ corresponds to perfect fringe contrast, while $\mathcal{V} = 0$ indicates complete loss of coherence. In principle, baselines of hundreds of meters to kilometers allow angular resolutions far beyond what any single aperture could achieve. This technique underlies modern facilities such as the Very Large Telescope Interferometer (VLTI) and the Center for High Angular Resolution Astronomy (CHARA) array [43, 44].

However, exploiting this technique at optical and near-infrared wavelengths imposes stringent requirements on phase coherence. Unlike radio interferometry, where the electric field can be directly digitized and time-stamped for offline correlation, optical detectors measure only intensity. The coherent combination of light from two

telescopes must therefore occur physically, by interfering the two beams on a beam splitter before detection. This turns the entire baseline into a large interferometer, in which the fringe visibility (Eq. 1.2) is exquisitely sensitive to the OPD between the two arms. A path length fluctuation of δL introduces a phase error of

$$\delta\phi = \frac{2\pi}{\lambda}\,\delta L, \tag{1.3}$$

which immediately reveals the severity of the problem: at optical wavelengths ($\lambda \sim 1\,\mu$m), a path length variation of just $\delta L = 100\,$nm already produces a phase error of $\delta\phi \approx 0.6\,$rad, sufficient to wash out a substantial fraction of the fringe contrast. Maintaining $\mathcal{V}$ above a practical threshold therefore requires the OPD to be held stable to tens of nanometers or better over the duration of an observation.

This is particularly challenging in practice because the optical path through each telescope arm includes contributions from atmospheric turbulence, mechanical vibrations of the telescope structure, and thermal expansion of the delay lines used to equalize the paths. Without active compensation, these perturbations cause the interference fringes to wash out on timescales of milliseconds, entirely destroying the coherence needed for high-resolution imaging. It is worth noting that this difficulty historically motivated an alternative approach known as Intensity Interferometry, pioneered by Hanbury Brown and Twiss [45], which circumvents phase requirements by correlating intensity fluctuations between telescopes rather than interfering the fields directly. While this technique is immune to atmospheric phase noise, it sacrifices the amplitude information that amplitude interferometry preserves, fundamentally limiting the angular resolution and sensitivity achievable.

Modern interferometric observatories therefore employ real-time fringe tracking systems: dedicated subsystems that measure the instantaneous OPD using a bright reference star and apply corrections via fast-steering mirrors or piezo-actuated delay lines, in a manner conceptually similar to the active phase stabilization architecture developed in this thesis. The GRAVITY instrument at the VLTI, for instance, achieves OPD residuals below $\sim 100\,\mu$rad by combining a fast metrology laser system with a high-bandwidth control loop, enabling the imaging of structures on sub-milliarcsecond scales [46].

The parallel between these examples is therefore direct: the physical quantity of interest, whether a secure key rate, spacetime dilation or a source image, is encoded in the optical phase, yet the detection process is inherently sensitive only to intensity. In the three cases, the degradation of phase coherence across a long optical baseline is the principal practical barrier, and demands active, real-time phase stabilization to function. This convergence of challenges across quantum networking, precision metrology and astronomical imaging underscores the broad scientific relevance of the stabilization techniques developed in this work.

1.2 Project Goals and Objectives

The practical realization of current quantum networking protocols, such as TF-QKD, relies entirely on the phase coherence of optical signals transmitted over long distances. However, optical fibers are inherently sensitive to environmental perturbations, such as thermal fluctuations and mechanical stress, which introduce severe phase noise and degrade signal integrity. The primary goal of this thesis is to tackle this challenge

by designing and implementing an active phase stabilization system for a distance-scalable Mach-Zehnder Interferometer (MZI). While the ultimate objective is to stabilize a deployed 10.8 km underground optical fiber link at Fermilab, this project focuses on developing and validating the underlying control architecture within a controlled laboratory testbed before field deployment.

A fundamental obstacle in achieving active stabilization is the ability to accurately measure the phase error in real-time. A standard MZI doesn't provide a direct measurement of the phase difference between its arms, as the output intensity only depends on the cosine of the phase difference, leading to ambiguity. To overcome this, we will implement a self-homodyne detection scheme that will allow us to extract the phase information directly.

Once the phase drift can be accurately measured, the system must be able to counteract these fluctuations rapidly. Because environmental noise, particularly acoustically induced jitter, can extend into high frequencies, traditional mechanical actuators lack the necessary bandwidth. Therefore, to physically correct the optical path length, we aim to integrate an EOM into the system. To orchestrate this, the final objective is the implementation of a low-latency digital control loop. By deploying a PID algorithm on a FPGA, the system will calculate the required corrections from the phase error signals and continuously drive the EOM in real-time. By combining these detection and control strategies, this project seeks to achieve robust, long-term phase locking, establishing a stable platform for future quantum communication endeavors.

Chapter 2

Theoretical Principles

This chapter will cover the fundamental concepts needed to understand the design and operation of the optical interferometer and its phase stabilization techniques presented in this thesis. It will begin with an overview of the Mach-Zehnder Interferometer (MZI) and its operating principles. From there, we are going to start building our setup, discussing the propagation of light in optical fibers, including the various noise mechanisms that can affect signal integrity. The chapter will then explore homodyne detection and the role of optical hybrids in coherent detection systems [42]. Next, we will examine phase modulation techniques using EOMs, which are crucial for controlling the phase of light in interferometric setups [47]. Finally, we will introduce FPGAs and their application in real-time signal processing for optical systems.

2.1 Mach-Zehnder Interferometer

The MZI is a widely used optical device first proposed by Ludwig Mach and Ludwig Zehnder in 1891 used for measuring the phase shift of light [48, 49, 50]. In their design, a beam of light is split into a sample arm and a reference arm, which are then recombined before hitting photodetectors (see Fig. 2.1). The intensities measured at the photodetectors will be different, since the electromagnetic fields will interfere constructively or destructively depending on the phase difference between the two arms.

The operation of the MZI can be described mathematically using the principles of wave interference [36]. When a coherent light source with an electric field amplitude E_0 is split at the first beam splitter, the fields in the two arms can be represented as:

$$E_1 = \frac{E_0}{\sqrt{2}} e^{i\phi_1}, \quad E_2 = \frac{E_0}{\sqrt{2}} e^{i\phi_2}, \tag{2.1}$$

where ϕ_1 and ϕ_2 are the phase shifts acquired in the sample and reference arms, respectively. Upon recombination at the second beam splitter, the resulting electric fields at the detectors can be expressed as:

$$E_{D1} = \frac{E_1 + E_2}{\sqrt{2}}, \quad E_{D2} = \frac{E_1 - E_2}{\sqrt{2}}. \tag{2.2}$$

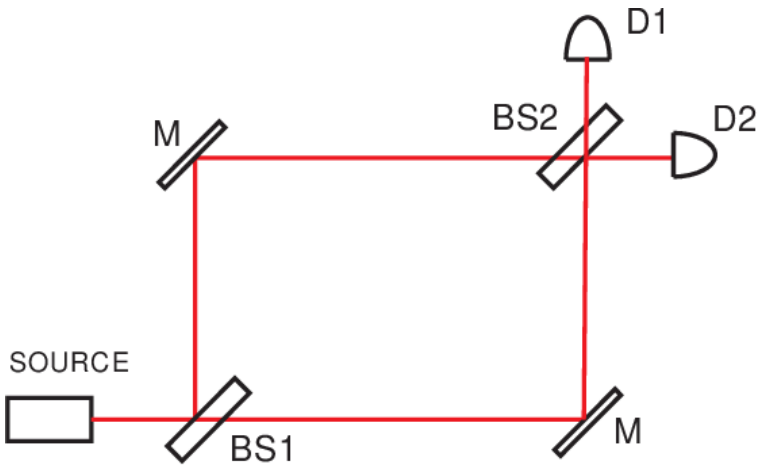

FIGURE 2.1: Schematic of a Mach-Zehnder Interferometer. A coherent light source is split into two arms by a beam splitter (BS1). The light in each arm is reflected by mirrors (M). The beams are then recombined at a second beam splitter (BS2), and the resulting interference pattern is detected by photodetectors (D1 and D2). The intensity at the detectors depends on the phase difference between the two arms.

The intensities at the detectors, which are proportional to the square of the electric field amplitudes, can be calculated as:

$$I_{D1} = |E_{D1}|^2 = \frac{E_0^2}{2}(1 + \cos(\Delta\phi)), \tag{2.3}$$

$$I_{D2} = |E_{D2}|^2 = \frac{E_0^2}{2}(1 - \cos(\Delta\phi)), \tag{2.4}$$

where $\Delta\phi = \phi_1 - \phi_2$ is the phase difference between the two arms. By measuring the intensities I_{D1} and I_{D2}, one can infer the phase difference $\Delta\phi$, which is sensitive to changes in the optical path length of the sample arm [51].

While the underlying principles are the same, our work utilizes a fiber-optic implementation of the MZI, where optical fibers are used to guide light through the interferometer arms. This approach offers several advantages, including compactness, flexibility, and ease of integration with other fiber-optic components. Nonetheless, optical fibers are also more susceptible to environmental perturbations, such as temperature fluctuations and mechanical vibrations, which can introduce phase noise and affect the stability of the interference pattern [52]. The following section will delve into the propagation of light in optical fibers and the associated noise that comes with it.

2.2 Optical Fiber Propagation and Noise Mechanisms

Optical fibers are utilized to easily guide light over long distances with minimal loss. They typically consist of a silica core with a high refractive index surrounded by a cladding with a lower refractive index, which confines the light within the core through total internal reflection, and a jacket that offers mechanical strength and physical protection (see Fig. 2.2).

The total internal reflection phenomenon comes from Snell's law (Eq. 2.5), which describes the behavior of light as it passes between two media with different refractive

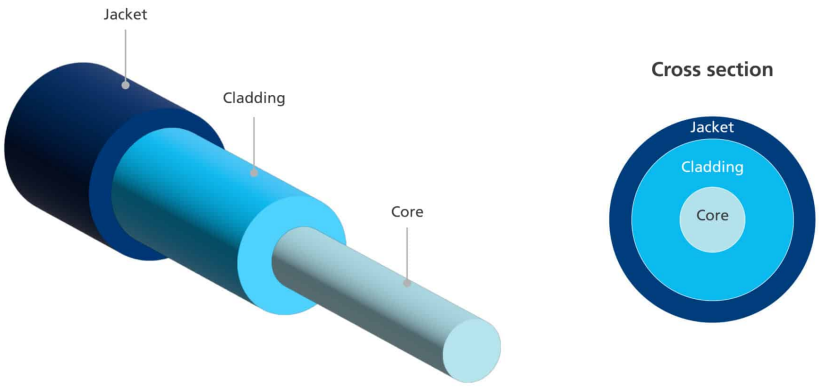

FIGURE 2.2: Structure of a typical optical fiber, showing the core, cladding, and jacket layers.

indices n_1 and n_2 with angle of incidence θ_1 and angle of refraction θ_2 [53]:

$$n_1 \sin(\theta_1) = n_2 \sin(\theta_2). \tag{2.5}$$

Figure 2.3 illustrates how total internal reflection occurs in an optical fiber when light traveling in the core hits the core-cladding interface at an angle greater than the critical angle, resulting in the light being reflected back into the core rather than refracted into the cladding, thus allowing efficient light propagation along the fiber.

The condition for total internal reflection is met when the incidence angle θ_1 exceeds the critical angle θ_c, defined as:

$$\theta_c = \arcsin\left(\frac{n_2}{n_1}\right). \tag{2.6}$$

While ray optics provides an intuitive understanding of light confinement, interferometric applications require a wave-optical description. In the context of this work, we utilize single-mode fibers. Single-mode fibers only support the fundamental spatial mode of a beam of light that propagates along the fiber axis [54]. The fiber is designed in a way that, for a specific cut-off wavelength, all higher-order fiber spatial modes are cut-off. The propagation of the electromagnetic field along the fiber axis (z) is governed by the effective refractive index of the mode, n_{eff}, and the propagation constant β:

$$\beta = \frac{2\pi}{\lambda} n_{eff}, \tag{2.7}$$

where λ is the vacuum wavelength of the laser source. Consequently, for a fiber of physical length L, the total accumulated optical phase ϕ is given by:

$$\phi = \frac{2\pi}{\lambda} n_{eff} L. \tag{2.8}$$

In an ideal scenario, ϕ would remain constant. However, in a real experimental environment, both the effective refractive index and the physical length are susceptible

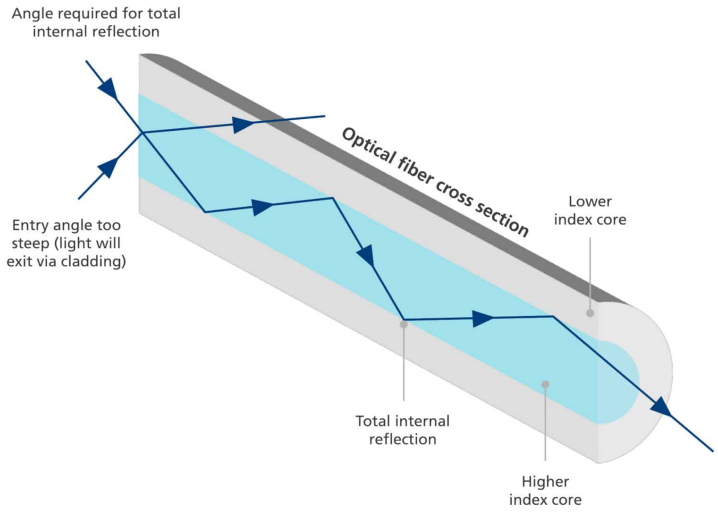

FIGURE 2.3: Illustration of total internal reflection in an optical fiber.

to external perturbations. They should be treated as functions of environmental parameters, primarily temperature (T) and mechanical stress (σ). Other factors, such as humidity and pressure, can also influence the fiber properties but typically have a much smaller effect compared to temperature and mechanical stress. Thus, we express n_{eff} and L as:

$$n_{eff} = n_{eff}(T, \sigma), \quad L = L(T, \sigma). \tag{2.9}$$

To quantify the instability of the interferometer, we consider the total differential of the phase, $d\phi$, which describes how infinitesimal changes in the environment propagate to the optical phase. Applying the chain rule to Eq. 2.8:

$$d\phi = \frac{\partial \phi}{\partial T} dT + \frac{\partial \phi}{\partial \sigma} d\sigma. \tag{2.10}$$

Substituting the definition of ϕ, we can expand the partial derivatives to identify the specific physical mechanisms contributing to the noise:

$$d\phi = \frac{2\pi}{\lambda} \left[\underbrace{\left(L \frac{\partial n_{eff}}{\partial T} + n_{eff} \frac{\partial L}{\partial T} \right)}_{\text{Thermoconductive effects}} dT + \underbrace{\left(L \frac{\partial n_{eff}}{\partial \sigma} + n_{eff} \frac{\partial L}{\partial \sigma} \right)}_{\text{Thermomechanical effects}} d\sigma \right]. \tag{2.11}$$

The first term in the brackets accounts for thermal phase noise, driven by the thermo-optic effect ($\partial n/\partial T$) and the thermal expansion of the silica ($\partial L/\partial T$). The second term describes acoustically induced noise, where mechanical vibrations stretch the fiber and alter the index via the elasto-optic effect [55]. These mechanisms introduce random phase drifts that the control system described in later chapters aims to suppress.

There are other intrinsic noise sources in optical fibers that can degrade signal quality, such as Rayleigh scattering and Brillouin scattering [56]. The first one arises

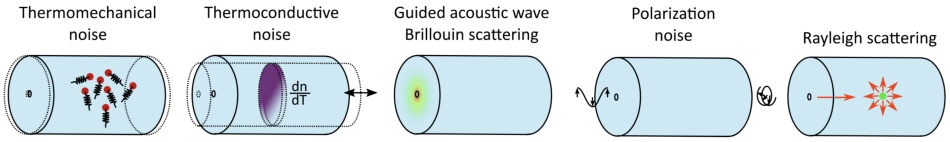

FIGURE 2.4: Overview of various noise sources affecting light propagation in optical fibers. Thermal fluctuations lead to changes in refractive index and fiber length, while mechanical vibrations induce strain and stress. Scattering processes such as Rayleigh and Brillouin scattering also contribute to signal degradation.

from density fluctuations in the fiber, causing light to scatter in various directions, while the second one results from the interaction of light with acoustic waves, leading to frequency shifts and additional noise components. Figure 2.4 provides an overview of these various noise mechanisms affecting light propagation in optical fibers. For short fibers, these effects are typically negligible compared to thermal and mechanical noise, but they become significant at long distances or high power levels.

There is also polarization noise, which arises from random fluctuations in the birefringence of the fiber due to environmental perturbations [57]. Birefringence is the property of a material where the refractive index varies depending on the polarization state of the light. In optical fibers, birefringence can be induced by asymmetries in the fiber core, external stresses, or temperature gradients. As light propagates through the fiber, these fluctuations can cause changes in the polarization state; if the polarization of the signal arm becomes misaligned with that of the reference arm at the point of interference, it can lead to reduced visibility and increased phase noise in the interferometric measurement. Consequently, control of the polarization state is crucial for maintaining high-fidelity signal detection in fiber-optic interferometers.

Given these propagation challenges and the stochastic nature of the noise sources, a simple intensity measurement is insufficient to fully characterize the optical signal. Instead, we require a coherent detection scheme that can extract both amplitude and phase information from the optical field. The next section will discuss homodyne detection, which is a widely used technique for achieving this goal.

2.3 Homodyne Detection

While the MZI principles described in Section 2.1 establish the fundamental relationship between phase difference and intensity (Eq. 2.4), standard interferometry presents a limitation: it yields a scalar measurement proportional to $\cos(\Delta\phi)$. This leaves an ambiguity in the sign of the phase and suffers from signal fading when $\Delta\phi$ approaches $k\pi$.

To overcome this, we employ a Balanced Homodyne Detection scheme utilizing a 90° Optical Hybrid [58]. This setup differs from the simple MZI in two key aspects: it utilizes a strong Local Oscillator (LO) to amplify the weak signal, and it extracts two orthogonal phase components simultaneously.

Homodyne detection allows us to measure the relative phase between the signal and the LO with high sensitivity. In a MZI, the LO is nearly identical to the signal, except for a small phase difference. Both arms carry the same noise coming from the

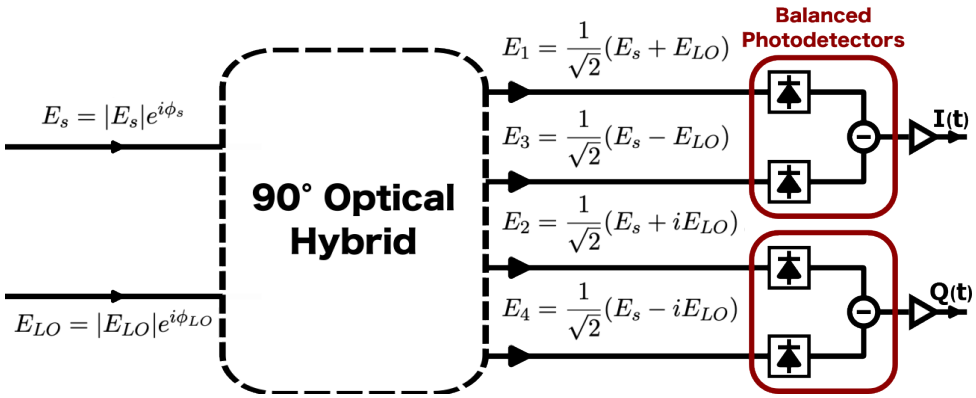

FIGURE 2.5: Schematic of a balanced homodyne detection setup. The incoming signal and local oscillator (LO) are combined in the hybrid, producing four outputs with relative phase shifts of 0°, 90°, 180°, and 270°. These outputs are then detected by two pairs of balanced photodetectors to extract the In-phase (I) and Quadrature (Q) components of the signal.

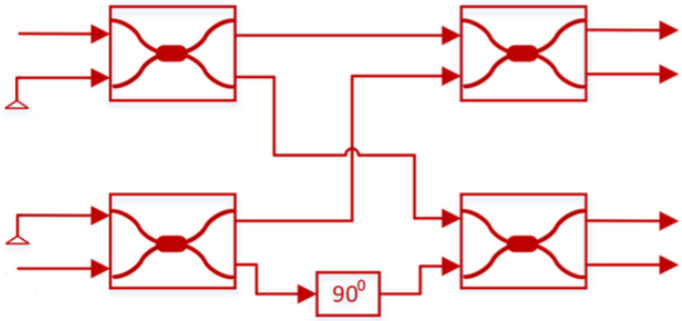

FIGURE 2.6: Schematic of a 90° Optical Hybrid architecture. The red boxes represent 50/50 beam splitters. There is a 90° phase shifter in one arm to create the required quadrature outputs.

laser source, since they are derived from the same beam. This is what we call common-mode noise and is a significant advantage of homodyne detection, as it allows us to effectively cancel out this noise during the detection process, improving the signal-to-noise ratio [59].

Figure 2.5 illustrates the configuration of a balanced homodyne detection setup. Both incoming signals mix at the hybrid to produce four outputs with relative phase shifts of 0°, 90°, 180°, and 270°. Figure 2.6 provides a detailed view of the optical hybrid's architecture. When the signal $\left(E_s = |E_s|e^{i\phi_s}\right)$ and the LO $\left(E_{LO} = |E_{LO}|e^{i\phi_{LO}}\right)$ combine at the hybrid, the resulting fields at the four outputs can be expressed as:

$$E_1 = \frac{1}{2}(E_s + E_{LO}), \tag{2.12}$$

$$E_2 = \frac{1}{2}(E_s + iE_{LO}), \tag{2.13}$$

$$E_3 = \frac{1}{2}(E_s - E_{LO}), \tag{2.14}$$

$$E_4 = \frac{1}{2}(E_s - iE_{LO}). \tag{2.15}$$

These optical outputs are coupled into two pairs of balanced photodetectors. Each pair measures the difference in photocurrents generated by the incident optical powers, effectively extracting two components of the signal.

For the In-phase component $I(t)$, we consider the outputs E_1 and E_3. The optical powers incident on the respective photodiodes are:

$$P_1 \propto |E_1|^2 = \frac{1}{4}|E_S + E_{LO}|^2 \tag{2.16}$$

$$= \frac{1}{4}\left[\underbrace{\left(|E_S|^2 + |E_{LO}|^2\right)}_{\text{Common-mode Noise}} + \underbrace{2\text{Re}\{E_S E_{LO}^*\}}_{\text{Interference Signal}}\right] \tag{2.17}$$

$$P_3 \propto |E_3|^2 = \frac{1}{4}|E_S - E_{LO}|^2 \tag{2.18}$$

$$= \frac{1}{4}\left[\underbrace{\left(|E_S|^2 + |E_{LO}|^2\right)}_{\text{Common-mode Noise}} - \underbrace{2\text{Re}\{E_S E_{LO}^*\}}_{\text{Interference Signal}}\right]. \tag{2.19}$$

The balanced detector subtracts these two photocurrents. Assuming identical responsivity $\mathcal{R}$ for both diodes, the resulting differential current i_I is:

$$i_I = \mathcal{R}(P_1 - P_3) = \mathcal{R}\text{Re}\{E_S E_{LO}^*\}. \tag{2.20}$$

Substituting the field definitions $E_S = |E_S|e^{i\phi_S}$ and $E_{LO} = |E_{LO}|e^{i\phi_{LO}}$, and defining the phase difference $\Delta\phi = \phi_S - \phi_{LO}$:

$$i_I = \mathcal{R}|E_S||E_{LO}|\cos(\Delta\phi). \tag{2.21}$$

Similarly, for the Quadrature component $Q(t)$, the balanced detector processes outputs E_2 and E_4. The 90° phase shift introduced by the hybrid (represented by the imaginary term in Eqs. 2.13 and 2.15) results in a sine dependence:

$$i_Q = \mathcal{R}(P_2 - P_4) = \mathcal{R}\text{Im}\{E_S E_{LO}^*\} = \mathcal{R}|E_S||E_{LO}|\sin(\Delta\phi). \tag{2.22}$$

Equations 2.21 and 2.22 highlight the critical advantage discussed earlier of balanced detection: the "common-mode noise" terms $|E_S|^2$ and $|E_{LO}|^2$, which carry the laser intensity noise, are mathematically cancelled out during the subtraction. This leaves only the interference terms, significantly improving the signal-to-noise ratio, and enabling precise phase information extraction.

2.3.1 Phase Recovery

With the orthogonal components i_I and i_Q available, the instantaneous phase error $\Delta\phi$ can be retrieved without ambiguity. Unlike the simple MZI intensity measurement, which is proportional only to $\cos(\Delta\phi)$, the homodyne system provides the full complex phasor vector (see Fig. 2.7). The phase is calculated via the four-quadrant arctangent function:

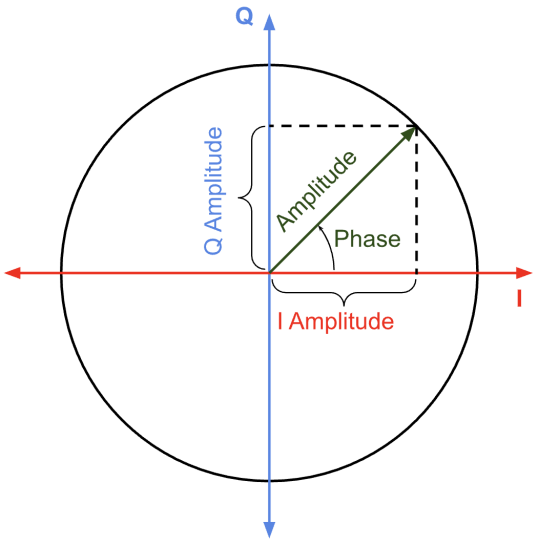

FIGURE 2.7: Phasor diagram illustrating the In-phase (I) and Quadrature (Q) components of the signal. The phase error $\Delta\phi$ is determined by the angle of the resultant vector formed by i_I and i_Q.

$$\Delta\phi(t) = \arctan\left(\frac{i_Q(t)}{i_I(t)}\right). \tag{2.23}$$

This method provides a linear response to phase changes and maintains constant sensitivity regardless of the absolute phase value. This calculated phase error $\Delta\phi(t)$ serves as the input variable for the PID control loop described in the following sections. The arctangent function's output lies within the range $(-\pi, \pi]$, which is suitable for small phase deviations around a setpoint (e.g., $\Delta\phi_{set} = 0$). However, for faster and larger phase excursions exceeding this range, phase unwrapping techniques must be employed to maintain continuity in the control signal [60].

Once the phase error is quantified, a compensatory mechanism is required to physically adjust the optical path length and close the feedback loop. This actuation is performed by an EOM, whose operating principles are detailed next.

2.4 Phase Modulation

Having established a method to precisely measure the optical phase error using homodyne detection, we will require an actuator capable of correcting these fluctuations in real-time. Given that environmental noise (particularly acoustically induced jitter) can extend into the kilohertz regime, mechanical actuators (such as piezo-electric fiber stretchers) often lack the necessary bandwidth. To achieve high-speed stabilization, we employ an EOM which takes advantage of the electro-optic effect.

This effect, also known as the Pockels effect, is a phenomenon where the refractive index of certain crystalline materials changes linearly in response to an applied electric field. Unlike the Kerr effect, which is quadratic, the Pockels effect provides a refractive index change Δn that is linearly proportional to the applied electric field E [61]:

$$\Delta n \approx -\frac{1}{2} n_0^3 r_{eff} E, \tag{2.24}$$

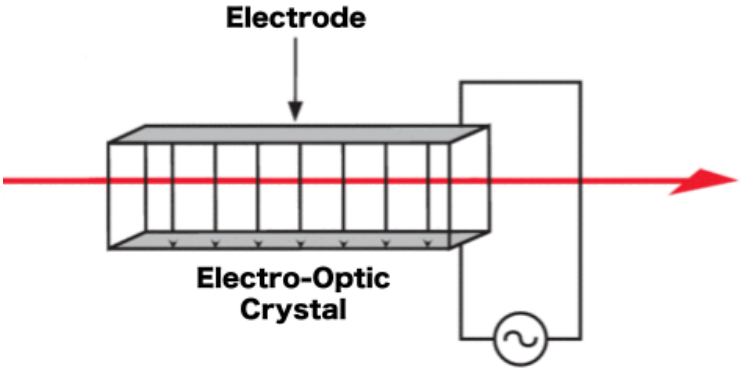

FIGURE 2.8: Schematic of an Electro-Optic Modulator (EOM). The applied voltage across the electrodes generates an electric field that modifies the refractive index of the crystal, thereby changing the optical path length for the light passing through it.

where n_0 is the unperturbed refractive index and r_{eff} is the effective electro-optic coefficient of the material depending on the crystal orientation and field direction.

In Fig 2.8 we can see a schematic representation of an EOM. It typically consists of a crystal (such as lithium niobate, $LiNbO_3$) with electrodes deposited on its surface. When a voltage V is applied across the electrodes, it generates an electric field $E = V/d$, where d is the distance between the electrodes. This field induces a change in the refractive index of the crystal, which in turn alters the optical path length for light propagating through it.

Starting from Eq. 2.8, the phase shift $\Delta\phi$ imparted to the light passing through the EOM can be expressed as:

$$\Delta\phi = \frac{2\pi}{\lambda}\Delta n L. \tag{2.25}$$

By substituting the expression for Δn, we find that the phase shift is a function of the applied voltage:

$$\Delta\phi(V) = \frac{\pi n_0^3 r_{eff} L}{\lambda d} V. \tag{2.26}$$

Equation 2.26 demonstrates that the optical phase can be linearly controlled by an applied voltage. However, physical EOMs and the Digital-to-Analog Converters (DACs) that drive them possess strict, finite voltage limits. Once the required control voltage exceeds the dynamic range of the hardware, the actuator will saturate, causing the control loop to rail and instantly lose the interferometric phase lock.

To achieve the desired robust, long-term phase locking, the control system must be capable of executing a phase unwrapping or fringe jump strategy. When the actuator nears its maximum voltage limit, the control logic inside the FPGA must rapidly reset the applied voltage by an exact ammount corresponding to a 2π phase shift, effectively "jumping" the phase back into the controllable range [62].

Consequently, active stabilization is reduced to a control loop problem: measuring the phase error (via homodyne detection), calculating the necessary correction taking the unwrapping into account, and applying the corresponding voltage to the EOM.

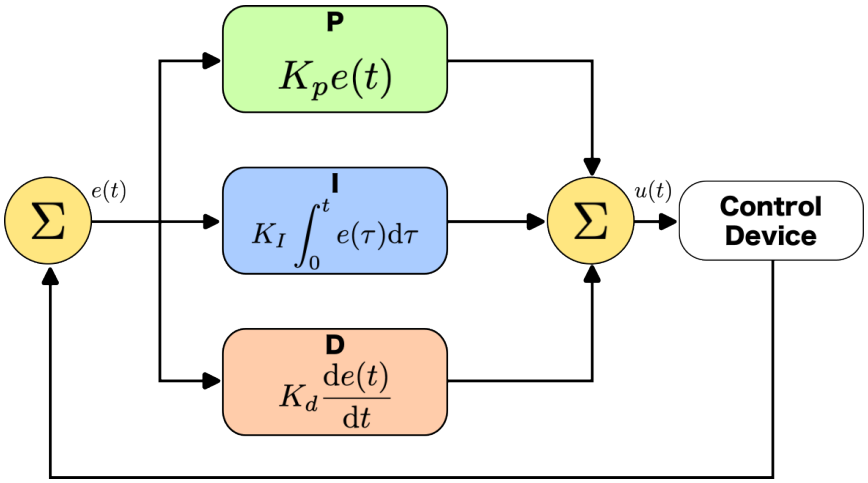

FIGURE 2.9: Illustration of the PID control loop. The measured phase error $e(t)$ is processed by the PID algorithm to generate the control signal $u(t)$, which is applied to a control device to correct the optical phase.

However, the efficacy of this feedback loop is strictly limited by its bandwidth and latency. Since environmental phase noise is a stochastic process occurring at high and low frequencies, the system must react with a delay significantly shorter than the noise coherence time. The next section will discuss the principles of feedback control necessary to achieve this.

2.5 Feedback Control Principles

An FPGA feedback control system is the final component required to stabilize the optical phase in the interferometer. In this work we worked with the Quantum Instrumentation Control Kit (QICK) group at Fermilab to build our experiment-specific control system [63]. The goal of the control loop is to maintain the phase difference $\Delta\phi(t)$ at a desired setpoint ϕ_{set} by continuously adjusting the voltage applied to the EOM based on real-time measurements from the homodyne detection scheme described in Section 2.3. The control loop needs an algorithm to compute the appropiate correction signal from the measured phase error, the most common of which is the PID algorithm, described next [64].

2.5.1 The PID Algorithm

The standard control loop architecture employed for phase locking is the PID controller. This algorithm calculates a correction signal $u(t)$ based on the history and trajectory of the error signal $e(t) = \phi_{set} - \Delta\phi(t)$. In the continuous time domain, the control function is defined as:

$$u(t) = K_p e(t) + K_i \int_0^t e(\tau)d\tau + K_d \frac{de(t)}{dt}, \tag{2.27}$$

where K_p, K_i, and K_d are the tunable gain coefficients for each term: The proportional term (K_p) produces a correction directly proportional to the current error, providing immediate response to disturbances. Too high of a value will lead to overshoot and oscillations. The integral term (K_i) accumulates past errors over time. This helps eliminate steady-state offsets but can introduce lag and instability if set too high.

The derivative term (K_d) reacts to the rate of change of the error, providing damping to suppress overshoot and ringing. However, it is sensitive to high-frequency noise and should be used judiciously.

Figure 2.9 illustrates the PID control loop. The calculated error phase is used to generate the control signal by using the weights found for each tunable gain coefficient. This control signal is then applied to the EOM to adjust the optical phase accordingly.

With that, now we have all the necessary components to understand the complete experimental setup. We have covered the principles of the MZI, the challenges of optical fiber propagation, the advantages of homodyne detection for phase measurement, the operation of EOMs for phase modulation, and the fundamentals of feedback control using a PID algorithm. The specific experimental implementation is detailed in the following chapter.

Chapter 3

Experimental Methods and Results

3.1 Experimental Setup

Following the theoretical framework established in the previous chapter, this chapter details the experimental implementation of the phase stabilization system. While the ultimate objective of this project was to stabilize a deployed 10.8 km underground fiber link, the development and validation of the control architecture were first conducted on a controlled laboratory testbed.

This approach allows for the isolation of specific noise sources and the optimization of the control loop parameters in a stable environment before field deployment. This chapter describes the experimental setup, the characterization of the optical channel using fiber spools to simulate long-distance scaling, the digital implementation of the feedback loop on an FPGA, and the final stabilization results.

To validate the active phase stabilization scheme, a fiber-optic MZI was constructed inside a noise-dampening box, built for passive phase noise reduction. It consists of a metallic structure with plastic walls and a foamed interior that absorbs vibrations and minimizes external disturbances. The experimental apparatus can be divided into three main subsystems: the optical layer (interferometer and fiber channel), the optoelectronic interface (modulation and detection), and the digital control logic.

3.1.1 Optical Layout

A schematic of the setup is shown in Fig. 3.1. The light source is a Continuous Wave (CW) laser **[Pure Photonics PPCL550]** operating at a central wavelength of 1536.6 nm with an advertised linewidth of 10 kHz. The linewidth ($\Delta\nu$) is a critical parameter for phase stabilization, as a narrower linewidth corresponds to a longer coherence length of the optical field ($L_c = c/\pi\Delta\nu$). With a linewidth of 10 kHz, the coherence length of our laser is approximately 9.5 km, which is sufficient for our laboratory testbed. The narrow linewidth ensures that the phase fluctuations we measure are predominantly due to environmental noise in the fiber rather than intrinsic laser noise, allowing us to effectively characterize and stabilize the interferometer.

The laser output is coupled into a single-mode fiber and directed to a 50:50 beam splitter (fiber coupler), which divides the optical power equally into two paths: the *Reference Arm* (LO) and the *Signal Arm*. The reference arm serves as the stable phase comparison for the interferometer, while the signal arm incorporates the fiber spools and the EOM for phase modulation. Both arms are designed to have similar optical power levels to ensure high interference visibility at the detection stage.

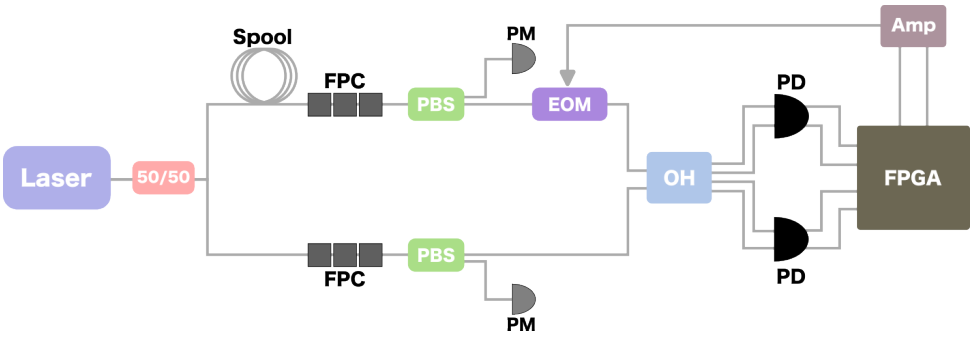

FIGURE 3.1: Schematic of the fiber-optic MZI used for phase stabilization. The setup consists of a CW laser source, a 50:50 fiber coupler to split the light into reference and signal arms. The signal arm can incorporate a optical-fiber spool to simulate longer distances. A Fiber Polarization Controller (FPC) is used to manage polarization right before a Polarizing Beam Splitter (PBS). We can monitor the power that goes into the detection stage using one arm of the Polarizing Beam Splitter (PBS) and a Power Meter (PM). The EOM is on the signal arm, right before the Optical Hybrid, where the two arms mix in order to obtain the four outputs. Each pair go into a Photodetector, where we obtain two signals for each detector. The detected signals are processed by a digital control system to generate feedback for the EOM for phase stabilization.

Reference Arm

The reference arm serves as the stable phase comparison for the interferometer. In this path, the light is routed through a second Fiber Polarization Controller (FPC) and Polarizing Beam Splitter (PBS) to align its polarization state with that of the signal arm. A Power Meter (PM) is included in both arms to monitor the optical power levels, which is critical for ensuring that the homodyne detection operates with high interference visibility and for diagnosing any power imbalances that could degrade the phase measurement sensitivity.

Signal Arm

The signal arm incorporates a set of optical fiber spools with lengths of 15, 30, and 45 meters. These spools introduce an optical path delay and attenuation, giving a simulation of the scalability of the interferometer.

Since standard single-mode fiber is not polarization-maintaining, the polarization state of the light evolves randomly as it propagates through the spools due to thermally and mechanically induced birefringence. To correct for this and ensure high interference visibility, a manual FPC is placed at the end of the spool. This is followed by a PBS, which acts as a polarization filter, ensuring that only light with a well-defined linear polarization state enters the detection stage.

Crucially, this arm houses the system's actuator: a Lithium Niobate ($LiNbO_3$) EOM **[EOSPACE]**. As detailed in Section 2.4, the EOM allows for high-bandwidth phase shifting in response to an applied voltage. By placing the EOM in the signal arm, the control loop can dynamically adjust the phase to track and cancel the fluctuations accumulated.

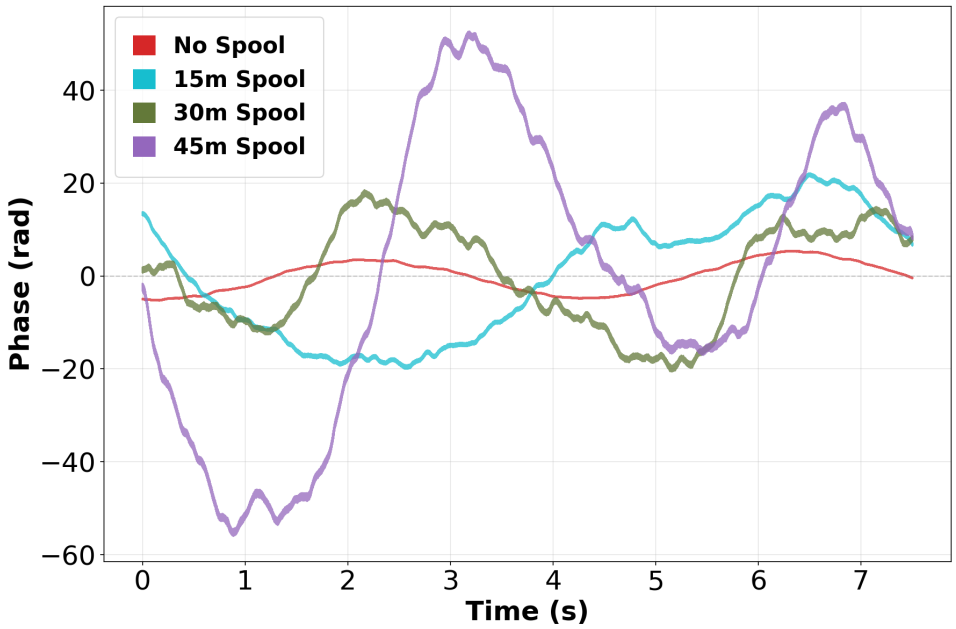

FIGURE 3.2: Free-running phase noise of the interferometer over a 7.5-second interval for 4 different configurations.

Configuration	Phase Standard Deviation (rad)
No spool	3.2886
15 meters spool	13.0973
30 meters spool	10.8655
45 meters spool	31.1137

TABLE 3.1: Standard deviation of the free-running phase noise for different configurations. The values indicate the level of phase fluctuations in the absence of active stabilization, with longer spools exhibiting higher noise levels due to increased environmental sensitivity.

Coherent Detection

The two arms are recombined at a 90° Optical Hybrid **[Optoplex HB-C0AFAS066]**. As described in Section 2.3, this passive component mixes the Signal and LO fields to produce four outputs with relative phase shifts. These outputs are coupled to a pair of amplified balanced photodetectors **[Thorlabs PDB425C]**, which give us two monitor outputs ($M_I^{+,-}$ and $M_Q^{+,-}$) each. These are voltage outputs that represent the individual optical power that each of the two internal photodiodes of each device receives. These allow us to perform the subtraction when going into the FPGA, yielding the In-phase (I) and Quadrature (Q) voltage signals required for processing.

Inside the FPGA, the I and Q signals are digitized and processed to extract the instantaneous phase $\phi(t)$ using the arctangent method and implementing the unwrapping logic. This phase information is then used to compute the error signal for the feedback loop, which is applied to the EOM to stabilize the interferometer.

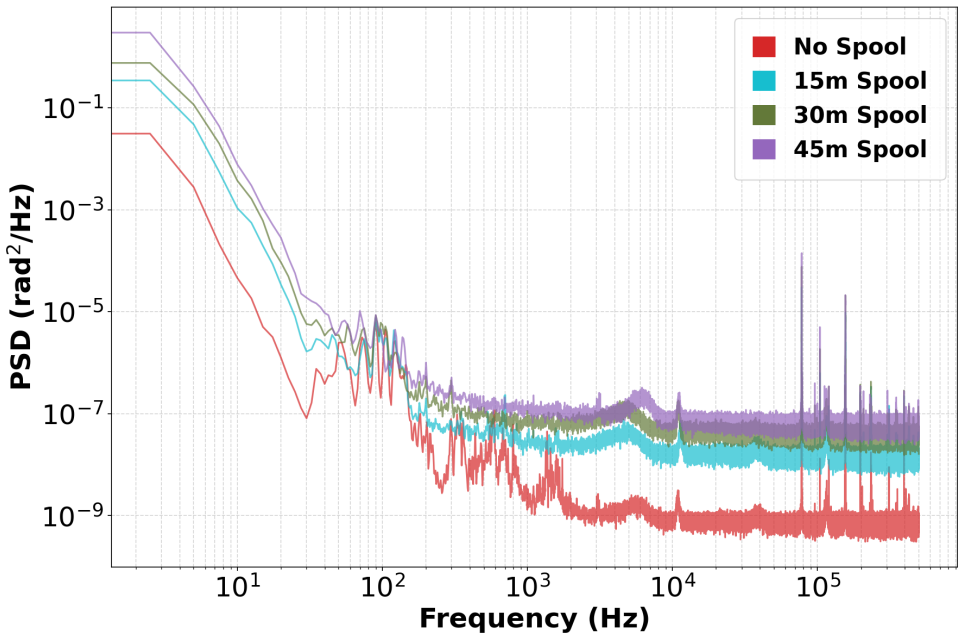

FIGURE 3.3: Power spectral density of the free-running phase noise for the same 4 configurations. The spectrum is dominated by low-frequency components associated with environmental perturbations affecting the fiber spools.

3.2 Performance Metrics and System Characterization

Before implementing the closed-loop control, the interferometer was characterized in an open-loop configuration to obtain a high interference visibility, and quantify the environmental phase noise baseline.

3.2.1 Free-Running Phase Noise

To establish a baseline for the control system performance, the interferometer was left in a "free-running" state (without active feedback) for a duration of 7.5 seconds. The instantaneous phase $\phi(t)$ was recovered from the digitized I and Q signals using the arctangent method described in Eq. 2.23.

When looking at Fig. 3.2, one can see that the system exhibited significant phase drift due to environmental perturbations. In Table 3.1, we summarize the standard deviation of the phase for each configuration, which quantifies the level of phase fluctuations in the absence of active stabilization. We can see that phase noise is a stochastic process in our results since the standard deviation does not monotonically increase with the spool length; the phase standard deviation of the 15 meters spool setup is larger than the 30 meters spool. Nevertheless, it is clear that longer spools exhibit higher noise levels due to increased environmental sensitivity. The no-spool configuration shows the lowest phase noise, while the 45 meters spool configuration exhibits the highest noise level, which is consistent with the expectation that longer fiber paths are more susceptible to environmental perturbations.

For this reason, plain phase standard deviation is not a sufficient metric to characterize the noise properties of the system. We will be using the PSD of the phase as a key metric to characterize the noise properties of the system, since it provides

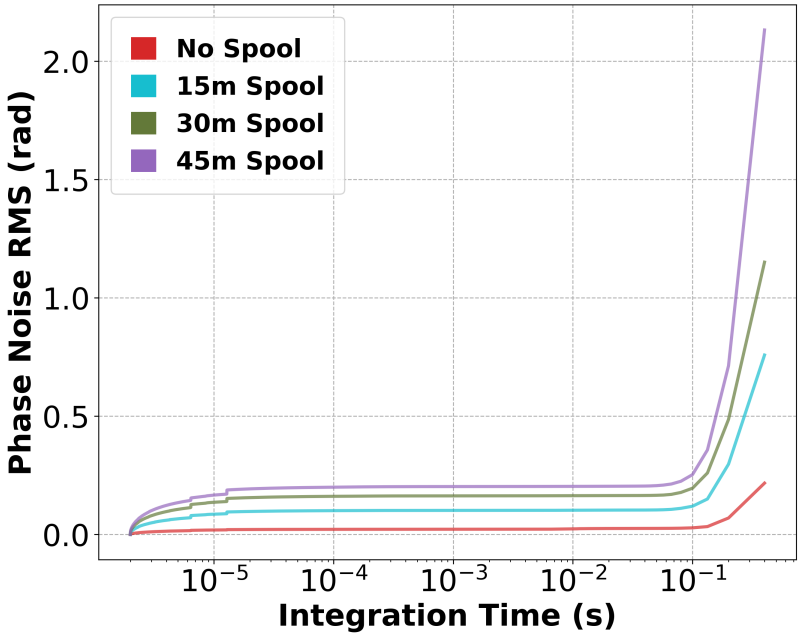

FIGURE 3.4: Integrated power spectral density of the free-running phase noise for the same 4 configurations.

Configuration	Phase RMS (rad)
No spool	0.30
15 meters spool	1.01
30 meters spool	1.53
45 meters spool	2.90

TABLE 3.2: Phase Root Mean Square (RMS) values obtained by integrating the power spectral density of the free-running phase noise for different configurations.

insight into the frequency components of the noise and allows us to identify dominant noise sources.

In the free-running case, the phase noise spectrum ($S_\phi(f)$) or PSD (see Fig. 3.3) is dominated by low frequency noise coming from environmental perturbations affecting the fiber spools. There is a clear bump in the spectrum of all configurations around 10^2 Hz, indicating the presence of a common noise source at that specific frequency. The noise floor at higher frequencies is orders of magnitude lower, which indicates that the dominant noise sources are indeed low-frequency environmental perturbations. The spectrum also shows that the noise level increases with spool length, which is consistent with the increased sensitivity to environmental disturbances.

Since the PSD represents the distribution of phase noise power across frequencies, the total area under the PSD curve represents the total phase noise. One can integrate the spectrum and take its square root to obtain the total phase Root Mean Square (RMS) as follows:

$$\Delta\phi_{\mathrm{RMS}} = \sqrt{\int_{\Delta\nu}^{1/\tau_{\mathrm{int}}} S_\phi(f)\mathrm{d}f}, \tag{3.1}$$

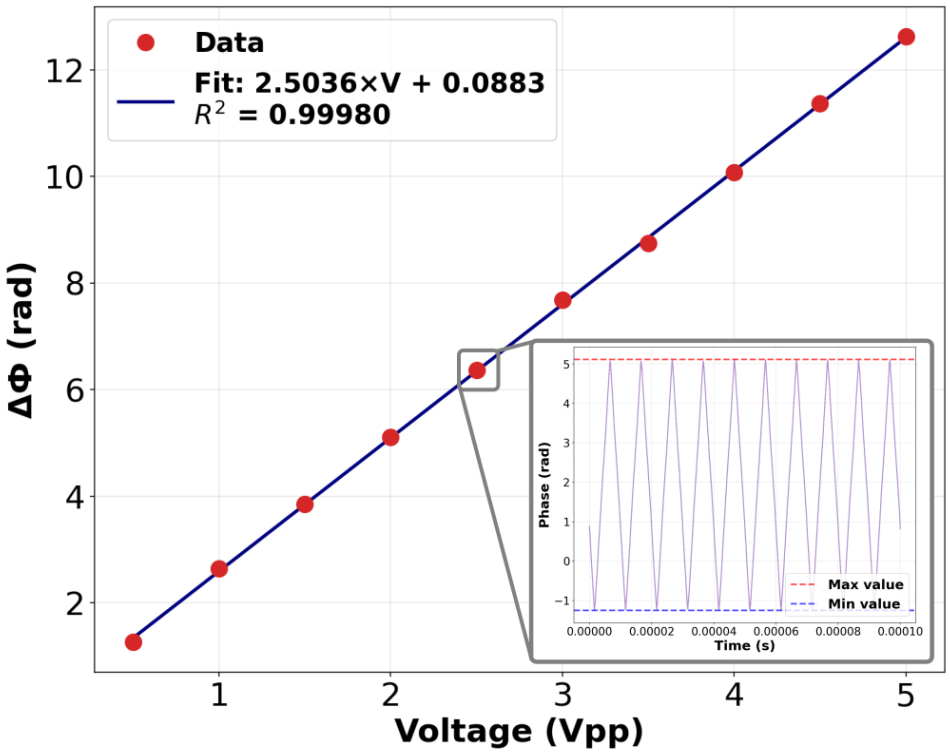

FIGURE 3.5: Calibration curve of the EOM showing the relationship between applied voltage and induced phase shift. The response function is extracted from the slope of the linear fit to the data points. An inset shows a zoomed-in view of one data point, illustrating the phase shift measurement process.

where $\Delta\nu$ is the bandwidth of the system and τ_{int} is the desired integration time. This allows us to quantify the total phase noise in terms of an RMS value, which is a critical metric for evaluating the performance of the stabilization system. Figure 3.4 shows the integrated PSD for the different configurations in the free-running case as a function of integration time.

Table 3.2 summarizes the final phase RMS values obtained by integrating the PSD over the entire bandwidth for each configuration. The results clearly indicate that the phase noise increases with the length of the fiber spool, which is consistent with the expectation that longer fiber paths are more susceptible to environmental perturbations.

3.2.2 EOM Calibration

Before implementing the feedback-loop, we need to calibrate the EOM to determine the voltage required to achieve a change in phase ($\Delta\phi(V)$), which is critical for setting the control loop parameters. This was done by applying 100 kHz voltage ramps of different amplitudes to the EOM using a function generator and measuring the resulting phase shift, taking the difference between the maximum and minimum phase values achieved. The calibration curve is shown in Fig. 3.5, where we can see a linear relationship between the applied voltage and the induced phase shift, which is expected for a well-behaved EOM. An inset in the figure shows a zoomed-in view of one data point, illustrating the phase shift measurement process.

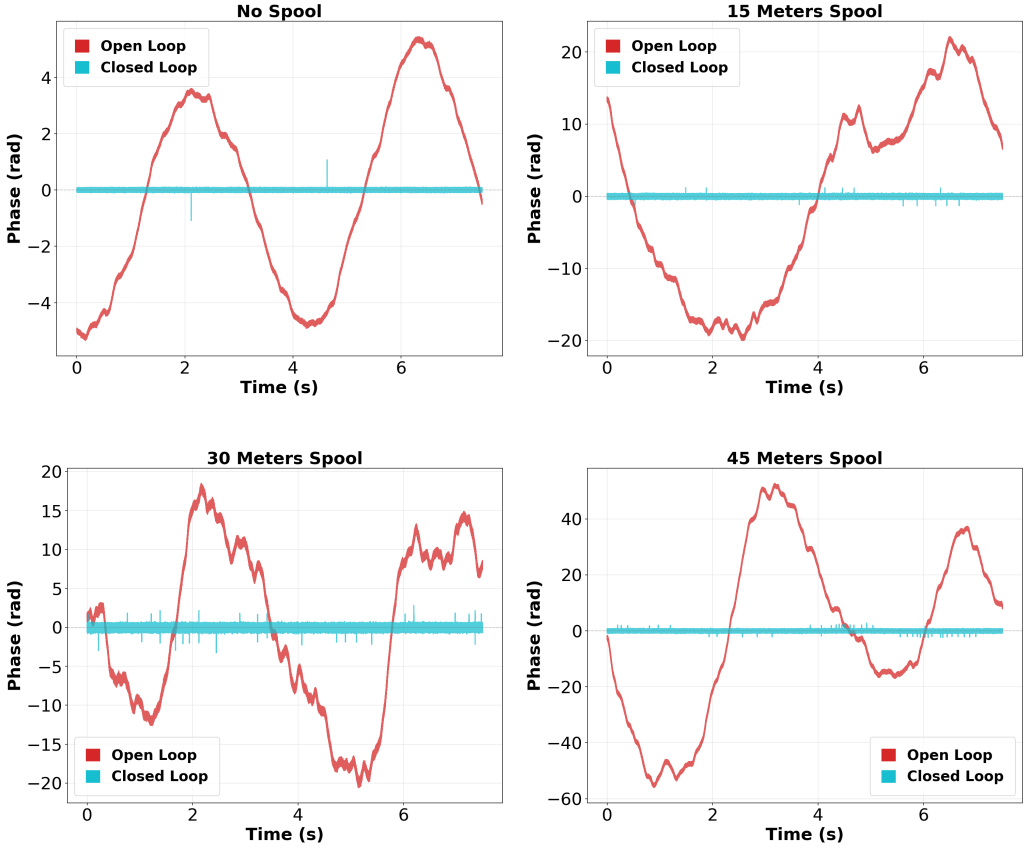

FIGURE 3.6: Closed-loop phase behaviour of the phase for different spool-length configurations. The active stabilization significantly reduces the phase drift and fluctuations compared to the open-loop case.

We can determine the response function from the slope of the linear fit applied to the data points, which takes V_{pp} values from 0.5 to 5 volts in steps of 0.5 volts. The extracted response function $\Delta\phi(V)$ is approximately $\mathbf{\Delta\phi = 2.5035 * V + 0.0883}$. This calibration curve is essential to prove our EOM has enough range for the proper functioning of the control loop, and to set the appropriate gain for the feedback system to ensure stability and optimal performance. Also, from the response function, we can extract the V_π value replacing $\Delta\phi$ with π, which give us approximately **1.256** V, indicating that a voltage of 1.256 V is required to achieve a π radian phase shift in our system.

3.3 Digital Control Implementation

The stabilization logic was implemented on an FPGA platform. This device serves as the central processing unit, handling signal digitization, phase error estimation, and feedback generation with deterministic low latency. The FPGA receives the digitized M_I^+ and M_I^- for the In-Phase (I) signal and M_Q^+ and M_Q^- for the Quadrature (Q) signal from the photodetectors, computes the instantaneous phase $\phi(t)$ using the arctangent method as seen in Eq. 2.23, and then calculates the phase error by comparing $\phi(t)$ to our setpoint (for which we tested $\phi_{set} = 0$ and $\phi_{set} = \pi$). The error signal is then processed through a digital PID controller, which computes the appropiate voltage

Configuration	Open-Loop StDev (rad)	Closed-Loop StDev (rad)
No spool	3.2886	**0.0246**
15 meters spool	13.0973	**0.1092**
30 meters spool	10.8655	**0.1947**
45 meters spool	31.1137	**0.2496**

TABLE 3.3: Standard deviation of the closed-loop phase noise for different configurations compared to the open-loop case. The results demonstrate a significant reduction in phase fluctuations due to the active stabilization, with the closed-loop system effectively maintaining the desired phase setpoint across all spool lengths.

correction to be applied to the EOM to counteract the measured phase fluctuations using the calibration performed.

3.3.1 PID Controller Tuning

The communication between the computer and the FPGA was established using a kerberized SSH connection, allowing for real-time monitoring and adjustment of the control parameters during testing. The PID controller parameters were tuned experimentally, ensuring that the system responds quickly to phase disturbances while maintaining stability. We followed a systematic approach to tuning, a method known as the Ziegler-Nichols method, which involves first setting the integral and derivative gains to zero and increasing the proportional gain until the system exhibits sustained oscillations. The critical gain and oscillation period were then used to calculate the appropiate values for the PID parameters using the following formulas [65]:

$$K_p = 0.6K_u, \tag{3.2}$$

$$K_i = 1.2K_u/T_u, \tag{3.3}$$

$$K_d = 0.075K_uT_u, \tag{3.4}$$

where K_u is the critical gain and T_u is the oscillation period. This tuning process was repeated iteratively, adjusting the parameters based on the observed system response to achieve optimal performance in terms of phase noise reduction and stability. The final tuned parameters were then used for the closed-loop performance evaluation, which is discussed in the next section.

3.3.2 Closed-Loop Performance

With the feedback loop active, the phase noise was measured again under the same conditions as the free running case. For the no-spool and the 15 meters spool configurations, the desired setpoint was $\phi_{set} = 0$, while for the 30 and 45 meters spools, we set $\phi_{set} = \pi$. For data analysis, we detrended the phase data by subtracting its mean value, so that the fluctuations around the setpoint were more clearly visible, and then we computed the standard deviation of the phase.

As shown in Fig. 3.6, the active stabilization significantly reduces the phase drift and fluctuations compared to the open-loop case. The phase distributions are more concentrated around zero, demonstrating that the control loop is succesfully maintaining the desired phase setpoint. The standard deviations (see Table 3.3) are much lower, indicating that the system is effectively tracking and compensating for the

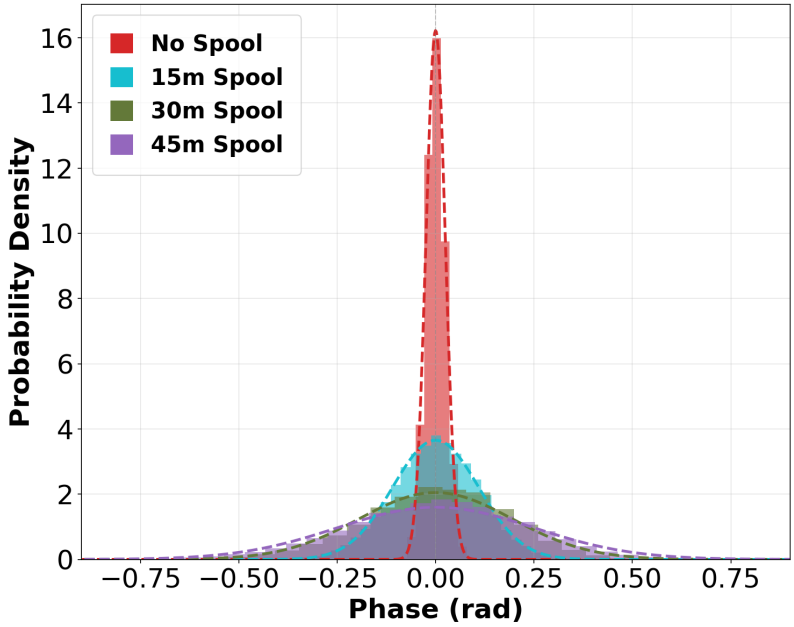

FIGURE 3.7: Histogram of the phase distributions for the closed-loop configurations.

phase noise. The no-spool configuration shows the best performance, with a standard deviation of only 0.0246 radians, a 99.25% phase noise reduction, while the 45 meters spool configuration has the highest standard deviation of 0.2496 radians, which is still a significant improvement compared to the open-loop case, since it yields a 99.20% reduction. These results demonstrate that the implemented feedback control system is effective in stabilizing the phase of the interferometer across all configurations, even in the presence of increased environmental sensitivity due to longer fiber spools.

Figure 3.7 shows the histogram of the phase distributions for the closed-loop configurations. The distributions are sharply peaked around zero, indicating that the control system is effectively suppressing phase excursions. The performance degrades as the spool length increases, which is expected due to the increased phase noise, but the control system still provides a significant improvement over the free-running case in all configurations.

Figure 3.8 shows a comparison of the phase Power Spectral Densities (PSDs) between the open-loop and the closed-loop configurations for the different spool lengths. The spectra show a significant reduction in low-frequency noise compared to the open-loop case, demonstrating the effectiveness of the active stabilization. The control loop effectively suppresses the low-frequency components of the phase noise, which were the most detrimental to our system performance. However, some residual noise remains at higher frequencies, which we can attribute to limitations in the control bandwidth. The results indicate that while the control system is effective in reducing phase noise, there are still areas for improvement, such as optimizing the controller parameters or implementing more advanced control strategies to further suppress high-frequency noise components. Overall, the results indicate that the implemented feedback control system is successful in stabilizing the phase of the interferometer.

A direct comparison of the PSD for all configurations is shown in Fig. 3.9, where we can see the significant improvement in phase noise performance across all spool

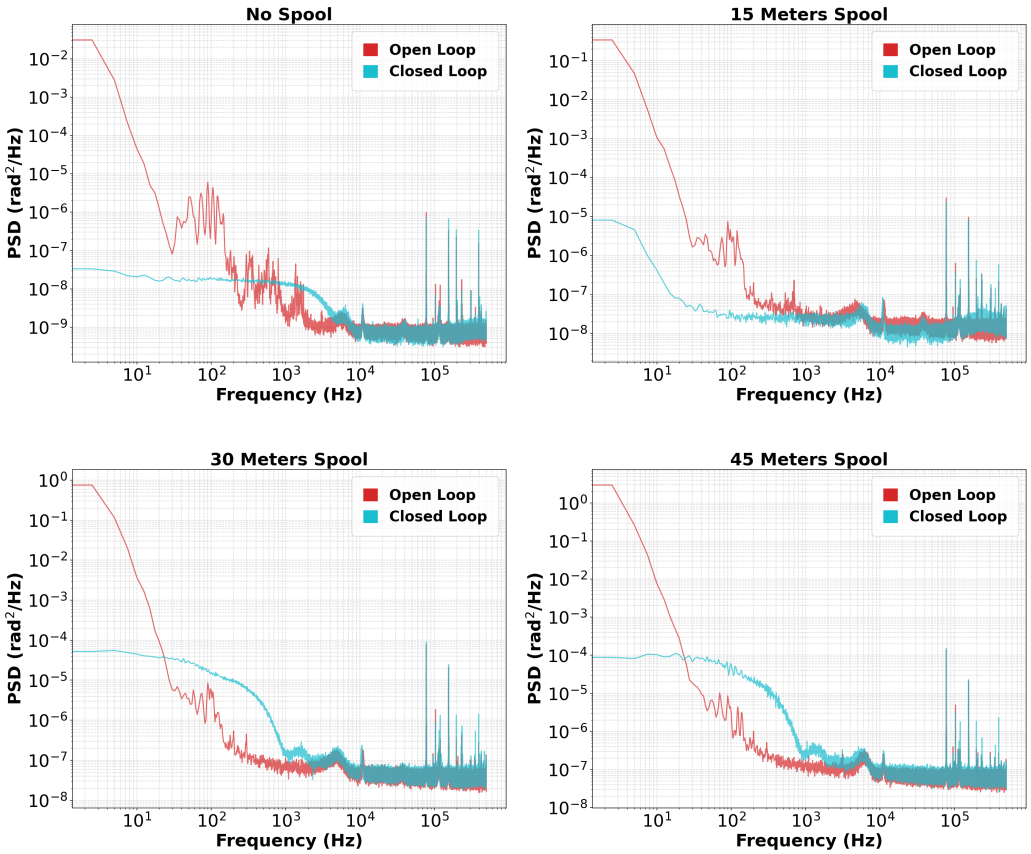

FIGURE 3.8: PSD of the closed-loop phase noise for different spool-length configurations. The spectra show a significant reduction in low-frequency noise compared to the open-loop case, demonstrating the effectiveness of the active stabilization.

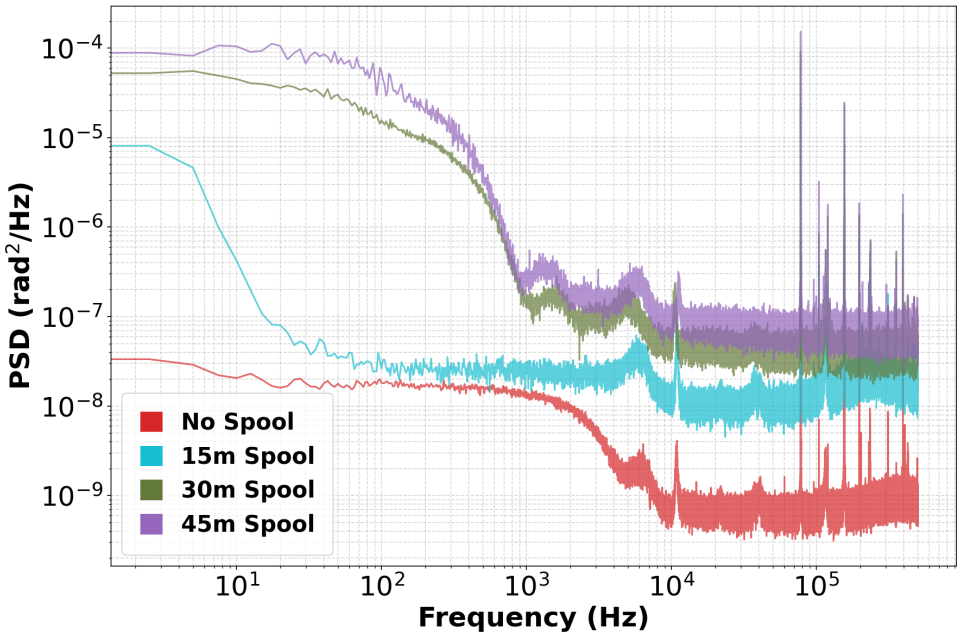

FIGURE 3.9: Comparison of the PSD of the closed-loop phase for all configurations.

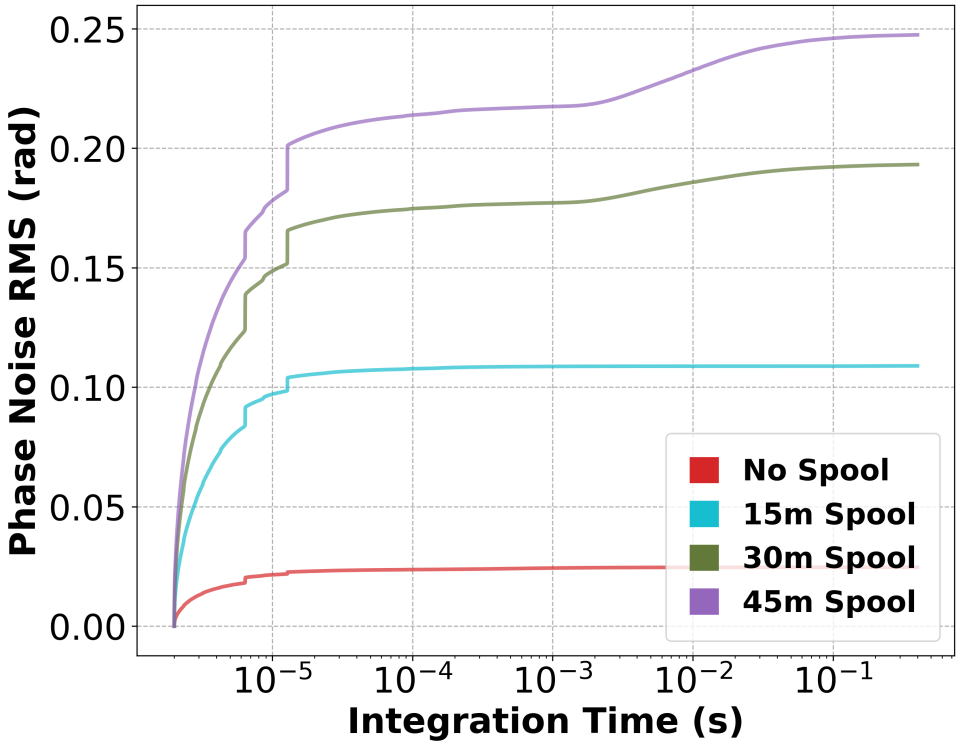

FIGURE 3.10: Integrated power spectral density of the closed-loop phase noise for the same 4 configurations.

Configuration	Open-Loop RMS (rad)	Closed-Loop RMS (rad)
No spool	0.30	**0.02**
15 meters spool	1.01	**0.11**
30 meters spool	1.53	**0.19**
45 meters spool	2.90	**0.25**

TABLE 3.4: Phase RMS values obtained by integrating the power spectral density of the closed-loop phase noise compared to the open-loop case for different configurations.

lengths, with the no-spool configuration showing the best performance as expected. The results demonstrate that the active stabilization scheme is effective in mitigating phase noise, even in the presence of increased environmental sensitivity due to longer fiber spools.

Figure 3.10 shows the integrated PSD for the closed-loop configurations. We can see that the active stabilization significantly reduces the total phase noise across all configurations compared to the free-running case. The results (see Table 3.4) indicate that the control system is effective in suppressing phase noise, particularly at low frequencies.

Chapter 4

Conclusion and Future Outlook

4.1 Synthesis of Empirical Findings

The primary objective of this thesis was to design, implement, and characterize an active phase stabilization system for a distance-scalable fiber-optic MZI. By employing a coherent self-homodyne detection scheme coupled with a 90-degree optical hybrid and a low-latency FPGA-based PID controller, the system successfully mitigated environmental phase noise in real time. The empirical results demonstrate a profound improvement in phase stability across various simulated distances. For the longest tested configuration utilizing a 45-meter fiber spool, the system reduced the highly volatile free-running phase standard deviation from 31.11 rad to a remarkably stable 0.25 rad under closed-loop control. Similarly, the integrated PSD confirmed a reduction in total RMS phase noise from 2.90 rad to 0.25 rad. These findings definitively validate that the high-bandwidth feedback loop effectively counteracts the low-frequency thermoconductive and thermomechanical noise sources inherent to silica fibers.

The system's performance was consistent across all tested configurations, with the most significant improvements observed in the longest fiber paths, which are typically more susceptible to environmental perturbations. This robust stabilization capability is crucial for applications such as quantum communication and precision metrology, where maintaining phase coherence over long distances is essential.

4.2 Theoretical Scalability to Real-World Implementation

While the laboratory testbed successfully demonstrated robust phase locking up to 45 meters, deploying this architecture across the target 10.8 km underground optical fiber link at Fermilab requires addressing additional scalability challenges. As the optical path length increases, the magnitude of environmental phase drift scales proportionally, placing greater demands on the dynamic range of the system's actuator. The Lithium Niobate EOM provides rapid, linear phase corrections, but possesses a strict, finite voltage limit characterized by its half-wave voltage, V_π.

A narrower linewidth laser source would be mandatory in order to test the system at the full deployed 10.8 km length, since the coherence length of the laser must exceed the total optical path length to maintain a stable interference pattern [66]. The current 10 kHz linewidth laser source, with a coherence length of approximately 9.5 km, is insufficient for testing the deployed configuration. A laser with a linewidth on the order of 1 kHz or less would be required to ensure a coherence length exceeding 10.8 km, allowing for effective phase stabilization over the full distance.

4.3 Contextualization and Future Directions

The empirical performance of the stabilization system can be directly contextualized within the operational requirements of modern quantum cryptographic protocols, particularly TF-QKD. TF-QKD exploits first-order single-photon interference at a central untrusted node to achieve secret key rates that scale with the square root of channel transmittance [33]. The security and efficiency of this protocol are inextricably linked to the interferometric visibility, $\mathcal{V}$, which is intrinsically degraded by residual phase noise.

The theoretical visibility is related to the RMS phase error by the approximation $\mathcal{V} \approx \cos(\Delta\phi_{RMS})$. Utilizing the 0.25 rad RMS phase error achieved in the 45-meter closed-loop configuration, the expected visibility is mathematically estimated as $\cos(0.25) \approx 0.9689$, or 96.9%. In QKD systems, the intrinsic Quantum Bit Error Rate (QBER) contributed solely by phase misalignment is given by $QBER \approx (1-\mathcal{V})/2$ [67]. Therefore, the residual phase noise of the current stabilization loop induces a baseline QBER of approximately 1.55%. This error rate is exceptionally low and comfortably below the theoretical security threshold of 11% required for secure key distillation in foundational protocols like BB84 [68]. By maintaining the phase coherence well within these strict cryptographic bounds, this active stabilization architecture proves its utility and establishes a highly viable hardware foundation for future long-baseline quantum networking experiments.

Looking ahead, several avenues for further research and development are apparent. A critical consideration for practical deployment is the coexistence of the classical stabilization signals and the quantum communication signals within the same fiber infrastructure. Since the active phase stabilization scheme relies on bright classical light co-propagating alongside single-photon-level quantum signals, managing the crosstalk between these two channels is essential to preserving the integrity of the quantum link. Recent work has begun addressing these coexistence challenges, demonstrating that classical and quantum signals can share the same fiber while maintaining high-fidelity quantum correlations [69]. Extending these findings to the Fermilab 10.8 km link will therefore be an important step towards integrating this stabilization system into a fully operational quantum network.

Enhancing the system's scalability to longer distances will be paramount, particularly in the context of the 10.8 km link at Fermilab. This will necessitate not only the implementation of a narrower linewidth laser but also potential refinements to the feedback control algorithms and PID parameter tuning methods to accommodate the increased complexity of longer fiber paths. Additionally, exploring alternative modulation techniques and materials may yield further improvements in phase stability and system performance. Finally, integrating this stabilization system into a complete quantum communication setup will be a critical step towards demonstrating its practical applicability in real-world quantum networks.

Bibliography

[1] Linus Pauling. *The nature of the chemical bond and the structure of molecules and crystals: an introduction to modern structural chemistry*. Vol. 18. Cornell university press, 1960.

[2] Felix Bloch. "Über die quantenmechanik der elektronen in kristallgittern". In: *Zeitschrift für physik* 52.7 (1929), pp. 555–600.

[3] Theodore H Maiman. "Stimulated optical radiation in ruby". In: *Nature* 187.4736 (1960), pp. 493–494.

[4] Albert Einstein. "Zur Quantentheorie der Strahlung". In: *Phys. Z.* 18 (1917), pp. 121–128.

[5] William Shockley. "Electrons and holes in semiconductors, with applications to transistor electronics". In: *(No Title)* (1950).

[6] Manuel Castells. *Information Age 3 Volume Set: Economy, Society and Culture*. 1999.

[7] A. G. J. MacFarlane, Jonathan P. Dowling, and Gerard J. Milburn. "Quantum technology: the second quantum revolution". In: *Philosophical Transactions of the Royal Society of London. Series A: Mathematical, Physical and Engineering Sciences* 361.1809 (2003), pp. 1655–1674. DOI: 10.1098/rsta.2003.1227.

[8] Serge Haroche. "Nobel Lecture: Controlling photons in a box and exploring the quantum to classical boundary". In: *Rev. Mod. Phys.* 85 (3 2013), pp. 1083–1102. DOI: 10.1103/RevModPhys.85.1083.

[9] David J. Wineland. "Nobel Lecture: Superposition, entanglement, and raising Schrödinger's cat". In: *Rev. Mod. Phys.* 85 (3 2013), pp. 1103–1114. DOI: 10.1103/RevModPhys.85.1103.

[10] Michel H Devoret and Robert J Schoelkopf. "Superconducting circuits for quantum information: an outlook". In: *Science* 339.6124 (2013), pp. 1169–1174.

[11] Richard P Feynman. "Simulating physics with computers, International journal of theoretical physics". In: *Int. J. Theor. Phys.* 21 (1982), pp. 467–488. DOI: 10.1007/BF02650179.

[12] J Aasi et al. "Advanced LIGO". In: *Classical and Quantum Gravity* 32.7 (Mar. 2015), p. 074001. ISSN: 1361-6382. DOI: 10.1088/0264-9381/32/7/074001. URL: http://dx.doi.org/10.1088/0264-9381/32/7/074001.

[13] A. André, A. S. Sørensen, and M. D. Lukin. "Stability of Atomic Clocks Based on Entangled Atoms". In: *Phys. Rev. Lett.* 92 (23 June 2004), p. 230801. DOI: 10.1103/PhysRevLett.92.230801. URL: https://link.aps.org/doi/10.1103/PhysRevLett.92.230801.

[14] Fabio Duarte. *Amount of data created daily (2025)*. Apr. 2025. URL: https://explodingtopics.com/blog/data-generated-per-day.

[15] Ronald L Rivest, Adi Shamir, and Leonard Adleman. "A method for obtaining digital signatures and public-key cryptosystems". In: *Communications of the ACM* 21.2 (1978), pp. 120–126.

[16] Arjen K Lenstra and Hendrik W Lenstra. *The development of the number field sieve*. Vol. 1554. Springer Science & Business Media, 1993.

[17] Peter W Shor. "Polynomial-time algorithms for prime factorization and discrete logarithms on a quantum computer". In: *SIAM review* 41.2 (1999), pp. 303–332.

[18] Davide Castelvecchi. "The race to save the Internet from quantum hackers". In: *Nature* 602.7896 (2022), pp. 198–201.

[19] Lily Chen et al. *Report on post-quantum cryptography*. Vol. 12. US Department of Commerce, National Institute of Standards and Technology . . ., 2016.

[20] Michele Mosca. "Cybersecurity in an era with quantum computers: Will we be ready?" In: *IEEE Security & Privacy* 16.5 (2018), pp. 38–41.

[21] Michael A Nielsen and Isaac L Chuang. *Quantum computation and quantum information*. Cambridge university press, 2010.

[22] Stephen Wiesner. "Conjugate coding". In: *SIGACT News* 15.1 (Jan. 1983), 78–88. ISSN: 0163-5700. DOI: 10.1145/1008908.1008920. URL: https://doi.org/10.1145/1008908.1008920.

[23] Charles H. Bennett and Gilles Brassard. "Quantum cryptography: Public key distribution and coin tossing". In: *Theoretical Computer Science* 560 (Dec. 2014), 7–11. ISSN: 0304-3975. DOI: 10.1016/j.tcs.2014.05.025. URL: http://dx.doi.org/10.1016/j.tcs.2014.05.025.

[24] Nicolas Gisin et al. "Quantum cryptography". In: *Reviews of Modern Physics* 74.1 (Mar. 2002), 145–195. ISSN: 1539-0756. DOI: 10.1103/revmodphys.74.145. URL: http://dx.doi.org/10.1103/RevModPhys.74.145.

[25] Gilles Brassard et al. "Limitations on Practical Quantum Cryptography". In: *Phys. Rev. Lett.* 85 (6 Aug. 2000), pp. 1330–1333. DOI: 10.1103/PhysRevLett.85.1330. URL: https://link.aps.org/doi/10.1103/PhysRevLett.85.1330.

[26] Won-Young Hwang. "Quantum Key Distribution with High Loss: Toward Global Secure Communication". In: *Phys. Rev. Lett.* 91 (5 Aug. 2003), p. 057901. DOI: 10.1103/PhysRevLett.91.057901. URL: https://link.aps.org/doi/10.1103/PhysRevLett.91.057901.

[27] Xiang-Bin Wang. "Beating the Photon-Number-Splitting Attack in Practical Quantum Cryptography". In: *Phys. Rev. Lett.* 94 (23 June 2005), p. 230503. DOI: 10.1103/PhysRevLett.94.230503. URL: https://link.aps.org/doi/10.1103/PhysRevLett.94.230503.

[28] Hoi-Kwong Lo, Xiongfeng Ma, and Kai Chen. "Decoy State Quantum Key Distribution". In: *Phys. Rev. Lett.* 94 (23 June 2005), p. 230504. DOI: 10.1103/PhysRevLett.94.230504. URL: https://link.aps.org/doi/10.1103/PhysRevLett.94.230504.

[29] Mirko Pittaluga. "Experimental implementation of Twin-Field Quantum Key Distribution Protocols". PhD thesis. Nov. 2022. URL: https://etheses.whiterose.ac.uk/id/eprint/31426/.

[30] W. K. Wootters and W. H. Zurek. "A single quantum cannot be cloned". In: *Nature* 299.5886 (Oct. 1, 1982), pp. 802–803. ISSN: 1476-4687. DOI: 10.1038/299802a0. URL: https://doi.org/10.1038/299802a0.

[31] Stefano Pirandola et al. "Fundamental limits of repeaterless quantum communications". In: *Nature Communications* 8.1 (Apr. 2017). ISSN: 2041-1723. DOI: 10.1038/ncomms15043. URL: http://dx.doi.org/10.1038/ncomms15043.

[32] H. J. Briegel et al. "Quantum repeaters for communication". In: (1998). arXiv: quant-ph/9803056 [quant-ph]. URL: https://arxiv.org/abs/quant-ph/9803056.

[33] Marco Lucamarini et al. "Overcoming the rate–distance limit of quantum key distribution without quantum repeaters". In: *Nature* 557.7705 (2018), pp. 400–403. DOI: https://doi.org/10.1038/s41586-018-0066-6.

[34] Shuai Zhao et al. "Phase-Matching Quantum Cryptographic Conferencing". In: *Phys. Rev. Appl.* 14 (2 Aug. 2020), p. 024010. DOI: 10.1103/PhysRevApplied.14.024010. URL: https://link.aps.org/doi/10.1103/PhysRevApplied.14.024010.

[35] M. Minder et al. "Experimental quantum key distribution beyond the repeaterless secret key capacity". In: *Nature Photonics* 13.5 (Mar. 2019), 334–338. ISSN: 1749-4893. DOI: 10.1038/s41566-019-0377-7. URL: http://dx.doi.org/10.1038/s41566-019-0377-7.

[36] Max Born and Emil Wolf. *Principles of optics: electromagnetic theory of propagation, interference and diffraction of light*. Elsevier, 2013.

[37] LIGO Scientific Collaboration et al. "Advanced ligo". In: *Classical and quantum gravity* 32.7 (2015), p. 074001. DOI: 10.1088/0264-9381/32/7/074001.

[38] Samuel M Brewer et al. "Al+ 27 quantum-logic clock with a systematic uncertainty below 10-18". In: *Physical review letters* 123.3 (2019), p. 033201. DOI: https://doi.org/10.1103/PhysRevLett.123.033201.

[39] Tobias Bothwell et al. "Resolving the gravitational redshift across a millimetre-scale atomic sample". In: *Nature* 602.7897 (2022), pp. 420–424. DOI: https://doi.org/10.1038/s41586-021-04349-7.

[40] K. Predehl et al. "A 920-Kilometer Optical Fiber Link for Frequency Metrology at the 19th Decimal Place". In: *Science* 336.6080 (2012), pp. 441–444. DOI: 10.1126/science.1218442. URL: https://www.science.org/doi/abs/10.1126/science.1218442.

[41] S. Droste et al. "Optical-Frequency Transfer over a Single-Span 1840 km Fiber Link". In: *Phys. Rev. Lett.* 111 (11 Sept. 2013), p. 110801. DOI: 10.1103/PhysRevLett.111.110801. URL: https://link.aps.org/doi/10.1103/PhysRevLett.111.110801.

[42] Kazuro Kikuchi. "Fundamentals of Coherent Optical Fiber Communications". In: *Journal of Lightwave Technology* 34.1 (2016), pp. 157–179. DOI: 10.1109/JLT.2015.2463719.

[43] John D Monnier. "Optical interferometry in astronomy". In: *Reports on Progress in Physics* 66.5 (2003), pp. 789–857. DOI: 10.1088/0034-4885/66/5/203.

[44] Theo A Ten Brummelaar et al. "First results from the CHARA array. II. A description of the instrument". In: *The Astrophysical Journal* 628.1 (2005), pp. 453–465. DOI: 10.1086/430729.

[45] R Hanbury Brown and Richard Q Twiss. "Correlation between photons in two coherent beams of light". In: *Nature* 177.4497 (1956), pp. 27–29. DOI: https://doi.org/10.1038/177027a0.

[46] Roberto Abuter et al. "First light for GRAVITY: Phase referencing optical interferometry for the Very Large Telescope Interferometer". In: *Astronomy & Astrophysics* 602 (2017), A94. DOI: 0.1051/0004-6361/201730838.

[47] Bahaa Saleh and Malvin Teich. *Fundamentals of Photonics, 2nd Edition*. June 2007. ISBN: 9780471358329.

[48] U. Grigull and H. Rottenkolber. "Two-Beam Interferometer Using a Laser". In: *J. Opt. Soc. Am.* 57.2 (Feb. 1967), pp. 149–155. DOI: 10.1364/JOSA.57.000149. URL: https://opg.optica.org/abstract.cfm?URI=josa-57-2-149.

[49] Ludwig Mach. "Ueber einen interferenzrefraktor". In: *Zeitschrift für Instrumentenkunde* 12.3 (1892), p. 89.

[50] Ludwig Zehnder. *"Ein" neuer Interferenzrefraktor*. Julius Springer, 1891.

[51] Yiwei Xie, Ming Zhang, and Daoxin Dai. "Design Rule of Mach-Zehnder Interferometer Sensors for Ultra-High Sensitivity". In: *Sensors* 20.9 (2020). ISSN:

1424-8220. DOI: 10.3390/s20092640. URL: https://www.mdpi.com/1424-8220/20/9/2640.

[52] Yanping Xu et al. "Vibration sensing using a tapered bend-insensitive fiber based Mach-Zehnder interferometer". In: *Opt. Express* 21.3 (Feb. 2013), pp. 3031–3042. DOI: 10.1364/OE.21.003031. URL: https://opg.optica.org/oe/abstract.cfm?URI=oe-21-3-3031.

[53] Eugene Hecht. *Optik*. Walter de Gruyter GmbH & Co KG, 2023.

[54] Govind P Agrawal. *Fiber-optic communication systems*. John Wiley & Sons, 2012.

[55] G. B. Hocker. "Fiber-optic sensing of pressure and temperature". In: *Appl. Opt.* 18.9 (May 1979), pp. 1445–1448. DOI: 10.1364/AO.18.001445. URL: https://opg.optica.org/ao/abstract.cfm?URI=ao-18-9-1445.

[56] Govind P. Agrawal. "Nonlinear Fiber Optics". In: *Nonlinear Science at the Dawn of the 21st Century*. Ed. by P. L. Christiansen, M. P. Sørensen, and A. C. Scott. Berlin, Heidelberg: Springer Berlin Heidelberg, 2000, pp. 195–211. ISBN: 978-3-540-46629-1. DOI: https://doi.org/10.1007/3-540-46629-0_9.

[57] I. Kaminow. "Polarization in optical fibers". In: *IEEE Journal of Quantum Electronics* 17.1 (1981), pp. 15–22. DOI: 10.1109/JQE.1981.1070626.

[58] Matthias Seimetz. *High-order modulation for optical fiber transmission*. Springer, 2009.

[59] G. Abbas, V. Chan, and Ting Yee. "A dual-detector optical heterodyne receiver for local oscillator noise suppression". In: *Journal of Lightwave Technology* 3.5 (1985), pp. 1110–1122. DOI: 10.1109/JLT.1985.1074301.

[60] Kazuyoshi Itoh. "Analysis of the phase unwrapping algorithm". In: *Appl. Opt.* 21.14 (July 1982), pp. 2470–2470. DOI: 10.1364/AO.21.002470. URL: https://opg.optica.org/ao/abstract.cfm?URI=ao-21-14-2470.

[61] Amnon Yariv and Pochi Yeh. *Photonics: Optical Electronics in Modern Communications*. Oxford University Press, 2007.

[62] Eric Udd and W.B. Spillman. *Fiber Optic Sensors: An Introduction for Engineers and Scientists: Second Edition*. July 2011. ISBN: 9780470126844. DOI: 10.1002/9781118014103.

[63] Leandro Stefanazzi et al. "The QICK (Quantum Instrumentation Control Kit): Readout and control for qubits and detectors". In: *Review of Scientific Instruments* 93.4 (Apr. 2022), p. 044709. ISSN: 0034-6748. DOI: 10.1063/5.0076249. eprint: https://pubs.aip.org/aip/rsi/article-pdf/doi/10.1063/5.0076249/19817152/044709_1_online.pdf. URL: https://doi.org/10.1063/5.0076249.

[64] Katsuhiko Ogata. "Modern control engineering". In: (2020).

[65] John G Ziegler and Nathaniel B Nichols. "Optimum settings for automatic controllers". In: *Transactions of the American society of mechanical engineers* 64.8 (1942), pp. 759–765.

[66] Joseph W Goodman. *Statistical optics*. John Wiley & Sons, 2015.

[67] Valerio Scarani et al. "The security of practical quantum key distribution". In: *Rev. Mod. Phys.* 81 (3 Sept. 2009), pp. 1301–1350. DOI: 10.1103/RevModPhys.81.1301. URL: https://link.aps.org/doi/10.1103/RevModPhys.81.1301.

[68] Peter W. Shor and John Preskill. "Simple Proof of Security of the BB84 Quantum Key Distribution Protocol". In: *Phys. Rev. Lett.* 85 (2 July 2000), pp. 441–444. DOI: 10.1103/PhysRevLett.85.441. URL: https://link.aps.org/doi/10.1103/PhysRevLett.85.441.

[69] Jordan M. Thomas et al. *Optimal filtering and generation of entangled photons for quantum applications in the presence of noise*. 2025. arXiv: 2510.06536 [quant-ph]. URL: https://arxiv.org/abs/2510.06536.